

1 **Glacial-interglacial shifts in dominant climate forcing over the last 33** 2 **ka in the northern South China Sea**

3 Xueqin Zhao^{*,1}, Shengjie Ye¹, Jiahui Yao¹, Michael E. Meadows^{2,3}, Chengyu Weng⁴, Yasong Wang¹,
4 Mingxing Zhang¹, Yunping Xu¹

5 ¹Shanghai Frontiers Research Center of the Hadal Biosphere, College of Oceanography and Ecological Science, Shanghai
6 Ocean University, Shanghai 201306, China

7 ²School of Geography and Ocean Sciences, Nanjing University, Nanjing 210023, China

8 ³Department of Environmental & Geographical Science, University of Cape Town, Cape Town 7701, South Africa

9 ⁴State Key Laboratory of Marine Geology, Tongji University, Shanghai, China

10 *Correspondence to:* Xueqin Zhao (xqzhao@shou.edu.cn)

11 **Abstract.** The northern South China Sea (SCS) is a critical region for understanding East Asian Monsoon dynamics. However,
12 integrated, multi-proxy records elucidating long-term climatic and vegetation changes in this region remain fragmented, with
13 a notable scarcity of coherent land-ocean interaction data during the Last Glacial Maximum (LGM). This gap has impeded
14 progress in elucidating the mechanisms underpinning monsoon variability and in rigorously evaluating the performance of
15 palaeoclimate models. To address this, we conducted a multi-proxy analysis combining palynological, organic- and inorganic-
16 geochemical methods on a marine sediment core from the northern SCS to reconstruct environmental and oceanic dynamics
17 at millennial-scale resolution that spans the last 33 ka. Our results reveal a clear contrast between glacial and interglacial
18 regimes. The glacial period, especially the LGM, was characterized by higher sedimentation rates, elevated marine primary
19 productivity, cooler and drier conditions, herb-dominated vegetation, and intensified fire activity. This regime was dominantly
20 forced by low sea level and glacial aridity, which together promoted open terrestrial vegetation and enhanced nutrient input to
21 the ocean. The deglaciation was characterized by pronounced warming, reduced productivity, increased moisture availability,
22 a shift to pine-dominated vegetation, and reduced fire activity. A key finding is the ocean warming which began around 1.3 ka
23 earlier than major terrestrial changes, indicating that tropical ocean-atmosphere interactions initiated the deglacial transition.
24 The overall findings highlight a fundamental transition in climatic controls, from a glacial regime dominated by sea-level-
25 driven shelf exposure and arid climate to an interglacial regime governed by tropical ocean-atmosphere dynamics. This study
26 underscores the sensitivity of the northern SCS to both high- and low-latitude forcing and the value of integrated land-sea
27 proxies in deciphering complex climate interactions.

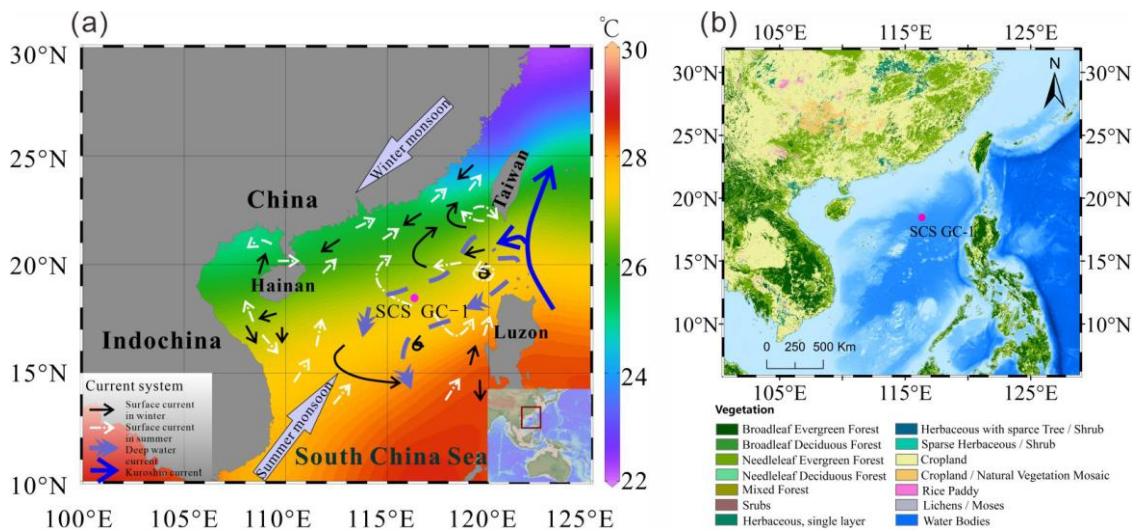
28 **1 Introduction**

29 Low latitude regions play a critical role in the global climate and its dynamic because they are the seat of the most active
30 moisture and heat exchanges between the atmosphere and the ocean expressed via the monsoon regime. Tropical and
31 subtropical monsoon regions such as East Asia and the South China Sea (SCS) experience the most significant seasonal
32 reversal in wind directions with associated migration of regional intense precipitation (Wang et al., 2017). Monsoon wind and
33 precipitation patterns have changed significantly in the late Quaternary, influenced by gradual changes in insolation and
34 internal interactions among the atmosphere, oceans, land surfaces and Northern Hemisphere ice sheets (An, 2000; Ding et al.,
35 1994; Kissel et al., 2020; Tian et al., 2010; Wang et al., 2001). These changes have affected the climate and land-ocean energy
36 balance of western Pacific marginal basins, whereas the influence and dynamics of the monsoon system remain insufficiently
37 constrained. Investigations of palaeoclimate variability have significant value in providing valuable insights into monsoonal
38 dynamics across tectonic, orbital and millennial time scales.

39 Given the importance of the climate signature during the last Glacial Maximum (LGM, spanning approximately 26.5-19 ka)
40 to climate model validation and testing, new reconstructions of precipitation and vegetation response during the LGM are

41 necessary to resolve inconsistencies and improve model reliability. Marine sediments potentially record the interplay of the
 42 East Asian Monsoon, surface and deep oceanic circulation and sea level compared with other terrestrial records (Tian et al.,
 43 2004; Wang et al., 1999). The South China Sea is divided into a northern deep basin with isolated, oxygen-poor waters and a
 44 southern extensive shelf province, a dichotomy fundamentally controlled by a ~2400 m deep sill that restricts deep-water
 45 exchange with the open Pacific (Chen and Huang, 1996). Due to its well-preserved sedimentary strata, abundant sediment
 46 supply, and relatively high sedimentation rates, the northern SCS is recognized as a key area with strong potential for high-
 47 resolution palaeoenvironmental reconstructions. Such records can substantially enhance our ability to resolve global and
 48 regional climate variability during the Quaternary (Wang et al., 2014). A range of different proxies is preserved in marine
 49 sedimentary archives. Pollen evidence, for example, can provide a valuable signal of vegetation evolution on the adjacent
 50 continental land mass (Cheng et al., 2023; Luo et al., 2016; Sun et al., 2000a), while microcharcoal particles are widely used
 51 in palaeofire reconstruction to infer fire frequency, intensity and vegetation changes, and terrestrial ecosystem response
 52 (Conedera et al., 2009). Foraminifera are sensitive to environmental changes, and are widely applied as a palaeo-proxy of
 53 marine conditions (Haynes, 1981), although the shells of planktonic foraminifera are susceptible to dissolution which may
 54 have limitations. Organic walled dinoflagellate cysts (dinocysts), the resting cysts formed during the sexual reproduction
 55 process of these taxa, are characterized by resistant organic matter and are also generally well preserved in marine sediments
 56 (Dale, 1996; Zonneveld et al., 2013). The well-known correlation of modern dinocyst distribution with distinct physical marine
 57 water properties such as sea surface temperature (SST), salinity, nutrients and productivity indicates the value of dinocysts as
 58 a proxy in palaeoceanographic reconstruction, although current research on dinocysts in the South China Sea remains largely
 59 confined to their modern distribution in marine surface sediments (Li et al., 2018a; Li et al., 2020; Li et al., 2023). Fossil
 60 dinocyst records in the SCS are scarce (Li et al., 2021; Li et al., 2017).

61 While previous studies have documented glacial-interglacial changes in vegetation and oceanography in the northern SCS, the
 62 relative importance of different forcing mechanisms-particularly the high- and low-latitude forcing across these transitions
 63 remain uncertain. To address this, we adopt a multi-proxy approach in this study, combining palynological indicators (pollen,
 64 spores, microcharcoal, and dinocysts), organic geochemical proxies (TOC and TN), and inorganic geochemical markers
 65 (element ratios, $\delta^{13}\text{C}$ and $\delta^{18}\text{O}$, and Mg/Ca-based SST of planktonic foraminifera) to reconstruct vegetation, fire regimes,
 66 sediment sources, ocean productivity, and sea surface temperature. A marine sediment core (SCS-GC-1; Fig. 1a) recovered
 67 from the northern SCS was analyzed to reconstruct millennial-scale climate and ocean dynamics over the last 33 ka. The
 68 specific aims of this study are: (1) to reconstruct the palaeovegetation and palaeoclimate; (2) to document the evolution of
 69 palaeoceanographic conditions; and (3) to clarify how land-ocean interactions and dominant climate forcings shift across
 70 glacial-interglacial transitions.



71
 72 **Figure 1:** (a) Map of the East Asian monsoon system and ocean circulations with annual modern mean annual sea surface
 73 temperature (Data from World Ocean Atlas, 2023) and the location of core SCS GC-1 (red) retrieved from the northern SCS.

74 (b) Map of the distribution of vegetation types in the main areas around the South China Sea retrieved from Stibig et al. (2007)
75 and <https://forobs.jrc.ec.europa.eu/products/glc2000/products.php>. The black solid line indicates the position of the winter
76 surface current, the white dashed line is the position of the summer surface current, the purple dashed line is the deep current,
77 and the blue solid line is the Kuroshio Current.

78 **2 Environmental setting**

79 **2.1 Atmospheric circulation and climate**

80 The northern SCS experiences a subtropical to tropical climate with high temperatures (15-28°C annually): the mean air
81 temperatures range from 15-25°C during the coldest month (January), and ~28°C during the warmest month (July). Rainfall
82 is copious with an annual mean of 1000-2000 mm (Li et al., 2017). The climate is primarily governed by the seasonal East
83 Asian Monsoon system: northeasterly winds prevail during winter (December-February) and southwesterlies dominate in
84 summer (June-August) (Chao et al., 1995; Wang et al., 2017). In winter, decreasing temperatures over the Asian continent lead
85 to the development and intensification of a cold high-pressure system over Inner Mongolia, while the Aleutian Low strengthens
86 over the North Pacific. The resulting continent-ocean pressure gradient drives the East Asian Winter Monsoon (EAWM),
87 transporting cold, dry northeasterly air masses southwards across China into the SCS. In summer, this pattern reverses: the
88 continental system is replaced by the Indian Low, and stronger high-pressure systems develop over the North Pacific and the
89 Australian region, generating the East Asian Summer Monsoon (EASM), which advects warm, moist-laden air from the ocean
90 onto the Chinese mainland (Liu et al., 2016a).

91 **2.2 Oceanic circulation**

92 Surface currents in the SCS are controlled by seasonal variations in the dominant wind directions related to the EASM and
93 EAWM (Hu et al., 2000), monsoon-topography interactions, and additional influences from wind-stressed eddies. During
94 winter, the EAWM drives a strong southward western boundary current along the Vietnamese and southern Chinese coasts,
95 associated with a basin-scale cyclonic circulation. In contrast, summer circulation is weaker and more complex, with coastal
96 currents generally reversing to flow northward under EASM influence.

97 The EASM drives distinct northern and southern circulation patterns in the SCS, which form two anticyclonic eddies separated
98 near 12°N by a strong upwelling off Vietnam (Fang et al., 1998). In addition, the region is influenced by the intrusion of warm,
99 saline Kuroshio waters entering through the Luzon strait between Luzon from Taiwan (Huang et al., 2025).

100 Seasonal variations in marine primary productivity are primarily modulated by the East Asian Monsoon (Liu et al., 2002).
101 During winter, stronger northeasterlies induce eutrophic conditions in the upper euphotic layer, elevating marine primary
102 productivity. In summer, persistent heating of warmer, lower-density surface waters intensifies stratification, leading to
103 oligotrophic conditions and reduced primary productivity (Liu et al., 2002; Zhang et al., 2016).

104 **2.3 Vegetation**

105 Vegetation types on the adjacent continental landmass around the SCS are diverse and reflect regional climate conditions (Luo
106 and Sun, 2013), although they are dominated by tropical and subtropical broadleaved evergreen forests (Fig. 1b) (Stibig et al.,
107 2007). Whereas tropical rain forest vegetation, characterized by taxa such as Dipterocarpaceae, Moraceae, Sapindaceae and
108 Sapotaceae, occurs at low altitudes on tropical islands along the southern coast of the Chinese mainland, e.g., Hainan Island,
109 and southern Taiwan Island. Tropical monsoon forests are distributed widely throughout the Indochina Peninsula and along
110 the coast of southeastern China with the representative species including Verbenaceae, Dipterocarpaceae, as well as pine trees
111 (including *Pinus merkusii*, *Pinus kesiya*, and *Pinus insularis*) which are dominant in the composition of monsoon mountain
112 forest. Subtropical evergreen forests, mainly composed of the families Fagaceae (e.g., *Cyclobalanopsis* and *Quercus*),
113 Lauraceae, and Theaceae, Hamamelidaceae and Magnoliaceae are prominent between 24°N and 25°N on southeast-facing
114 hills and on high plateaus (Wang, 1961; Whitmore, 1985). Generally, the abundance of both tropical and subtropical taxa

115 increase gradually towards the south in eastern China, indicating the significance of the north-south temperature gradient (Dai
116 and Weng, 2015; Dai et al., 2015). The vegetation types occurring in southeast and southern China, as well as Taiwan Island,
117 are the main pollen sources of the northern SCS (Dai and Weng, 2011; Sun et al., 1999).

118 **2.4 Sedimentation rates**

119 The SCS receives enormous amounts of terrigenous sediments (ca. 700×10^6 tons/year) every year, mainly during the rainy
120 season in summer. The sediments originate from the erosion/weathering of rocks in the catchment basins particularly from
121 three Asian rivers (the Red River, the Pearl River, and the Mekong River) which are among the largest in the world (Liu et al.,
122 2010; Milliman and Syvitski, 1992). Beyond the river deltas, part of the terrigenous sediments is deposited on the shelves
123 (Zhong et al., 2017), while the rest reaches the open sea where the sediment is transported by the oceanic currents and deposited
124 on the continental slope and in the deep basins (Liu et al., 2013).

125 **3. Materials and methods**

126 **3.1 Materials and chronological analysis**

127 The 305 cm long marine sediment core SCS GC-1 was retrieved from the northern SCS during R/V Songhang (Shanghai
128 Ocean University) cruise in October 2022 (18.47°N, 116.34°E; water depth of 3764 m) (Fig. 1).

129 Eight accelerator mass spectrometry AMS ^{14}C dates at depths of 20 cm, 45 cm, 65 cm, 90 cm, 107 cm, 133 cm, 203 cm and
130 275 cm were obtained on mixed planktic foraminiferal (including *Globigerinoides ruber*, *Globigerinoides sacculifer*,
131 *Neogloboquadrina dutertrei*, *Pulleniatina obliquiloculata*, *Orbulina universa*) tests isolated from the core. AMS ^{14}C
132 measurements were carried out on a NEC 0.5Mev ^{14}C AMS (National Electrostatics Corporation, NEC) at Guangzhou Institute
133 of Geochemistry, Chinese Academy of Sciences (GIGCAS).

134 **3.2 X-ray fluorescence (XRF) analysis**

135 The core was non-destructively scanned using the Avaatech XRF Core Scanner at the State Key Laboratory of Marine Geology,
136 Tongji University. The parameters of the Avaatech XRF core scanner were set for 30 s exposure time, three voltage and current
137 conditions with 10 kv and 0.75 mA for Al-Fe, 30 kV and 0.5 mA for Co-Mo, and 50 kV and 0.2 mA for Tc-U. The scanning
138 area was 5 mm (length) \times 10 mm (width), and at a scanning time of 30 s. The relative content of each element including Al to
139 Ba which was obtained, is expressed in cps as counts per second.

140 **3.3 TOC and TN analysis**

141 Approximately 1 g of each freeze-dried sample was treated with diluted 3 mol/L HCl for 24 hours at room temperature to
142 remove inorganic carbonates. After the reaction, the samples were repeatedly rinsed with ultrapure water ($>18 \text{ M}\Omega \cdot \text{cm}$) and
143 centrifuged until the supernatant reached a neutral pH. The remaining residue was oven-dried at 60°C, ground and then
144 weighed. The decarbonated samples were analyzed for elemental content using a Vario EL cube elemental analyzer (Elementar,
145 Germany) at the State Key Laboratory of Marine Geology, Tongji University, employing the dry combustion method.
146 Replicate analyses were conducted to ensure data reliability, with average standard deviations of ≤ 0.1 wt% for both TOC and
147 TN measurements.

148 **3.4 Planktonic foraminiferal isotopic and Mg/Ca analysis**

149 The samples were freeze-dried, disaggregated by soaking in water for 1-2 days, then were rinsed repeatedly through a 63 μm
150 sieve to remove organic matter and fine impurities. The rinsed wet samples were then dried at 60°C (approximately 24 h) and
151 passed through a 125 μm and 250 μm sieve, respectively (Schönfeld et al., 2012). *G. ruber* larger than 250 μm size were

152 selected under a microscope. For each sample, clean and intact *G. ruber* (around 30 specimens) were picked and tested using
153 a Finnigan MAT253 Mass Spectrometer. The $\delta^{18}\text{O}$ results are reported versus VPDB after calibration with NBS 19. The
154 average test accuracy is $\pm 0.07\%$.

155 For the Mg/Ca analysis, surface dwelling foraminiferal species with smooth-surface individuals of *G. ruber* between 250-350
156 μm (ca. 0.3 mg) were picked to ensure no obvious contamination or damage, and that the atrioventricular structure was intact
157 (Barker et al., 2003). The analysis was performed on a quadrupole inductively coupled plasma mass spectrometry (ICP-MS).
158 Duplicate measurements of two samples yield an average relative deviation of 0.064 mmol/mol, confirming that analytical
159 uncertainty is minimal and does not materially affect interpretation. Sea surface temperatures were reconstructed following
160 Eq. (1) (Huang et al., 2008):

$$161 \text{ SST} = 0.5 * (\ln(\text{Mg/Ca}/0.3)/0.09 + \ln(\text{Mg/Ca}/(0.38 - 0.02 * D)))/0.09 \quad (1)$$

162 Where SST represents mean annual sea surface temperature ($^{\circ}\text{C}$), Mg/Ca is the *G. ruber* based Mg/Ca ratio (mmol/mol), D is
163 water depth of the core (km).

164 3.5 Palynological analysis

165 In total, 61 samples (mean interval 4 cm) were processed for palynological analysis at Shanghai Ocean University following
166 standard preparation procedures. Samples were treated sequentially with 10% HCl, 40% HF, 30% HCl, sieved with 125 μm
167 and 7 μm meshes, and mounted for microscopic examination. Routine identification was performed under a light microscope
168 (ZEISS Promostar 3) at 400x magnification, with 1000x used for detailed taxonomic identification. Four *Lycopodium* spore
169 tablets with 10315 ± 845 spores were added to each sample prior to processing to enable calculation of pollen concentration.
170 Pollen taxa were identified using the reference of Tang et al. (2020). At least 300 pollen grains (including terrestrial pollen
171 taxa, sedges and aquatic taxa) were counted for most of the samples. The percentages of pollen taxa were calculated based on
172 the pollen sum excluding *Pinus*, and the percentages of spore taxa were calculated based on pollen and spore sum. The 95%
173 confidence intervals of percentages were calculated following Maher (1972).

174 Charcoal particles were identified and counted on the same microscope slides prepared for pollen analysis. Only particles
175 which were black, opaque and angular were considered as charcoal. Particles smaller than 10 μm were not counted due to the
176 risk of false identification (Mooney and Tinner, 2011). More than 1500 charcoal particles (with an average of 3500 particles)
177 were counted for each sample. Two size classes were defined, based on the length of the long axis of each fragment: 10-100
178 μm is assumed to relate to the regional fire signal and $>100 \mu\text{m}$ to local fire signals (Conedera et al., 2009).

179 Organic-walled dinoflagellate cysts (dinocysts) were identified based on Zonneveld et al. (2013), DINOFLAJ3 (Williams et
180 al., 2017), and the online modern dinocyst determination key, viz Zonneveld and Pospelova (2015) and references therein. The
181 percentage of each taxon was calculated based on the total number of dinocysts. The 95% confidence intervals of percentages
182 were calculated following Maher (1972). All identified dinocyst taxa and their motility affinities are listed in Table S1. In
183 addition to the above content, foraminiferal organic linings, and other non-pollen palynomorphs such as fungal spores were
184 counted. All counts of pollen, microcharcoal and dinocysts as well as other data discussed in this study have been submitted
185 in the Pangaea database (<https://pangaea.de>) (Felden et al., 2023).

186 3.6 Statistical analysis

187 The pollen and dinocyst data were analyzed statistically using the CANOCO software (Canonical Community Ordination:
188 version 5) (ter Braak and Smilauer, 2012). The percentage data used for statistical analysis was not transformed. A Detrended
189 Correspondence Analysis (DCA) was first conducted to test the distribution of the dataset (unimodal or linear). The longest
190 gradient of DCA analysis was found to be 1.1 for pollen data and 1.5 for dinocyst data with standard deviations both less than
191 3, suggesting that the linear model is more suitable. Accordingly, separate Principal Component Analysis (PCA) were
192 performed to determine the relationship between relative abundances of pollen and dinocyst taxa. Assemblage zones were
193 determined using the constrained cluster analysis (CONISS) in the TILIA (3.0.1) software (Grimm, 2015), which were
194 performed separately, for the pollen (based on a sum excluding *Pinus*) and dinocyst taxa. The top two samples were excluded
195 from the dinocyst CONISS analysis due to insufficient dinocyst counts.

196 **4. Results**

197 **4.1 Age-depth model**

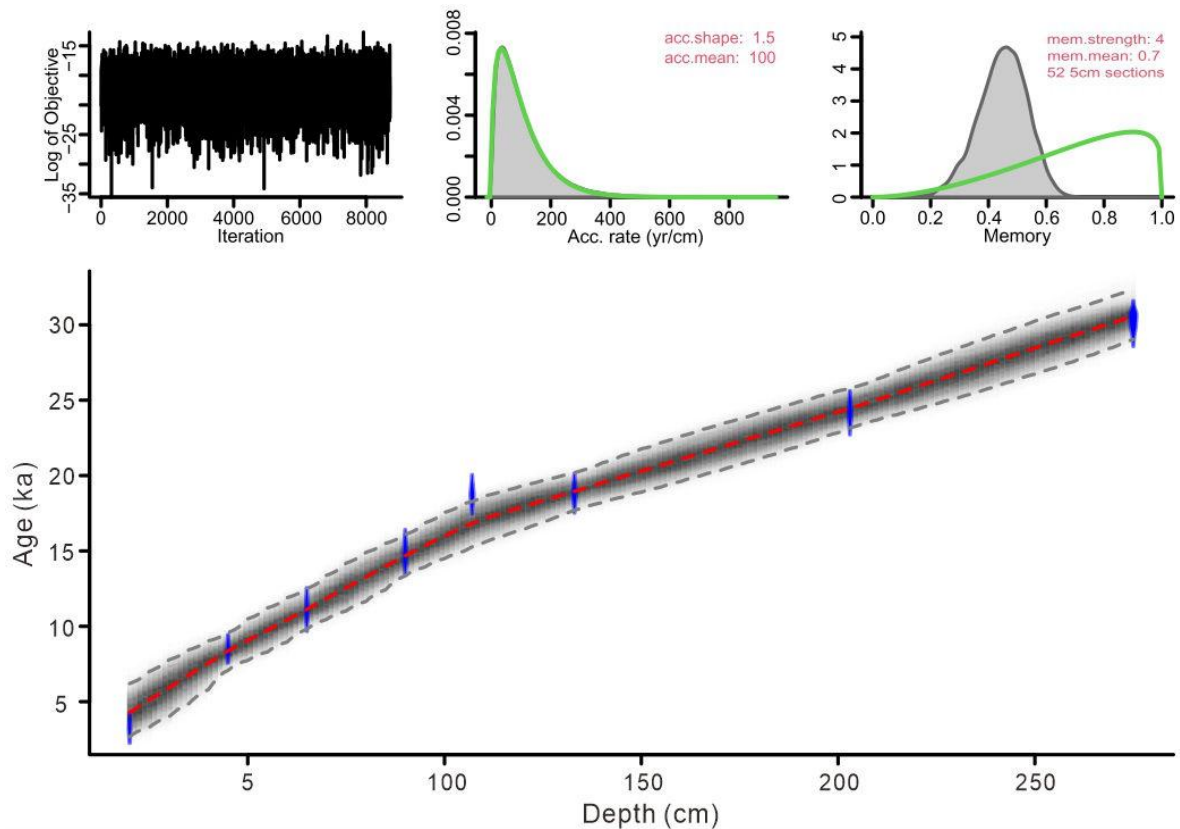
198 The eight ^{14}C AMS measurements exhibit a systematic increase in radiocarbon age with sediment depth (Table 1). The age-
199 depth model was constructed using the eight AMS ^{14}C measurements in a Bayesian framework implemented in Bacon (Blaauw
200 and Christen, 2011). A prior accumulation rate of 100 yr/cm (shape = 1.5, normal distribution) was applied, with the core
201 divided into 52 depth sections of 5 cm. The default memory parameter was retained. Posterior weighted mean calibrated ages
202 were used to derive linear sedimentation rates. The resulting model indicates a basal age of ~ 33 ka for core SCS GC-1, with
203 sedimentation rates ranging between 0.005 and 0.013 cm/yr (Figs. 2 and 3a).

204

205 **Table 1:** AMS ^{14}C measurement for mixed planktonic foraminifera from the core SCS GC-1.

Lab #	Depth (cm)	Material	^{14}C age (yr BP)	Calibrated age median (cal. yr BP)	cal. ^{14}C age (cal. yr BP, $\pm 2\sigma$)
GZ10650	20	mixed species	3420 \pm 25	3036	1810-4285
GZ10651	45	mixed species	8005 \pm 35	8289	7260-9443
GZ10652	65	mixed species	10055 \pm 50	10868	9533-12260
GZ10653	90	mixed species	13090 \pm 70	14708	13392-16057
GZ10654	107	mixed species	15950 \pm 70	18342	17138-19485
GZ10655	133	mixed species	16000 \pm 90	18399	17185-19555
GZ10656	203	mixed species	20540 \pm 170	23656	22496-24875
GZ10657	275	mixed species	26700 \pm 350	29977	28806-31063

206 # yr BP denote before present (1950 AD); all age data were calibrated using the software Calib.Rev.8.10 (Stuiver and Reimer,
207 1993) and Marine 20 (Hughen et al., 2004). The standard marine reservoir age with a local modification ($\Delta R = 71 \pm 499$ yr) in
208 the northern South China Sea was applied (Wan and Jian, 2014).

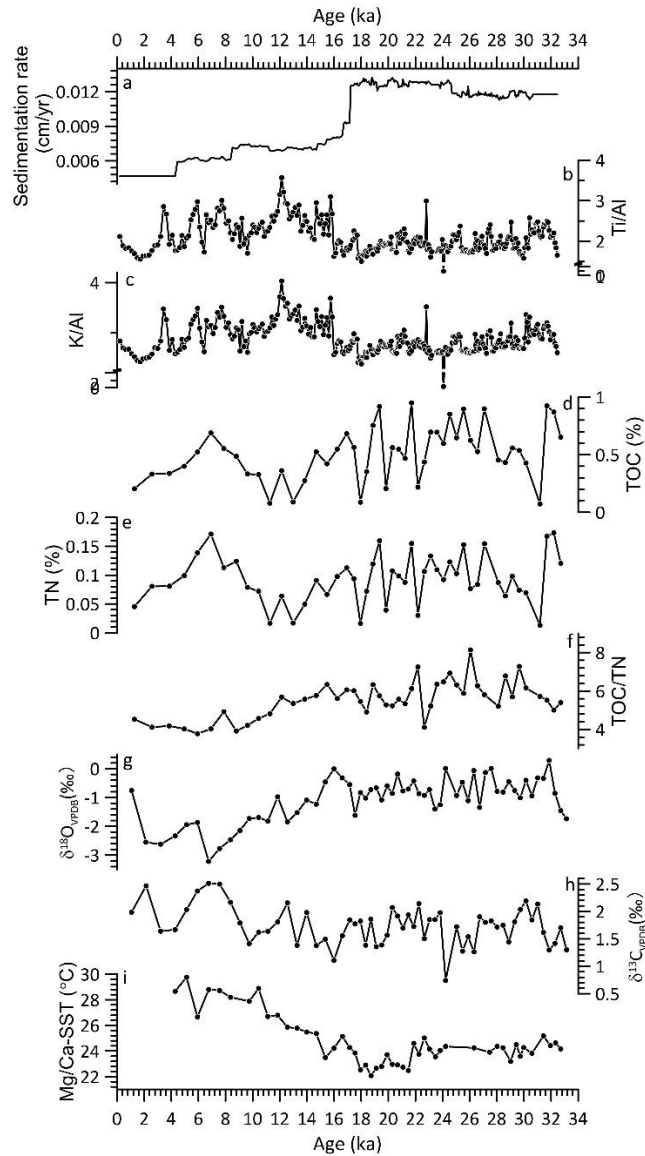


209

210 **Figure 2:** Bayesian age-depth model based on eight AMS ^{14}C dates from core SCS GC-1: the blue areas represent the 95%
 211 probability distributions of the calibrated ages; the thin red line shows the weighted mean ages, and the blackish-gray area
 212 shows the 95% age-depth relations as modeled by the R software package Bacon 2.2 (Blaauw and Christen, 2011).

213 4.2 XRF record

214 The relative contents of these six elements are found for Fe (5×10^3 - 750×10^3 cps, mean = 540×10^3 cps), Ca (0.7×10^3 - 650×10^3
 215 cps, mean = 190×10^3 cps), K (1.5×10^3 - 166×10^3 cps, mean = 91×10^3 cps), Si (1×10^3 - 144×10^3 cps, mean = 71×10^3 cps)
 216 followed by Ti (2×10^3 - 68×10^3 cps, mean = 41×10^3 cps) and Al (0.5×10^3 - 14×10^3 cps, mean = 6×10^3 cps) (Fig. S1). Similar
 217 patterns among terrigenous elements Fe, K, Ti, Al and Si were observed together with a clearly opposite pattern of marine
 218 origin element Ca. The Ti/Al and K/Al show similar patterns with significant correlation ($r = 0.94$, $P < 0.001$) throughout the
 219 record (Figs. 3b and 3c), with low values prior to 16 ka and then increase quickly to much higher values after 16 ka with
 220 gradually decreasing trend to the end of the record.



221

222 **Figure 3:** Core SCS GC-1 sedimentation rate (a), major element ratio (b-c), contents of total organic carbon (TOC, d) and
 223 nitrogen (TN, e), TOC/TN ratio (f), stable oxygen isotope $\delta^{18}\text{O}_{\text{VPDB}}$ (g) and stable carbon isotope $\delta^{13}\text{C}_{\text{VPDB}}$ (h) isotopes of
 224 planktic foraminifera, and Mg/Ca-SST (i).

225 4.3 TOC, TN and TOC/TON record

226 TOC content and the TOC/TN ratio exhibit significant fluctuations throughout the record (Figs. 3d, 3e and 3f). The period
 227 prior to 14.7 ka is characterized by high TOC content with low values around 31.2 ka, 22.2 ka, 19.8 ka, 17.9 ka. After 14.7 ka,
 228 TOC decreased until 10.4 ka when it increased again to a high level around 6.9 ka followed by a decline trend until the top of
 229 the record. Similarly, TOC/TN ratio also exhibits high values prior to 14.7 ka, which then decreased to minimum between 8.8-
 230 5.9 ka interrupted by a brief increase around 7.9 ka.

231 4.4 Planktonic foraminiferal isotopic and Mg/Ca-SST record

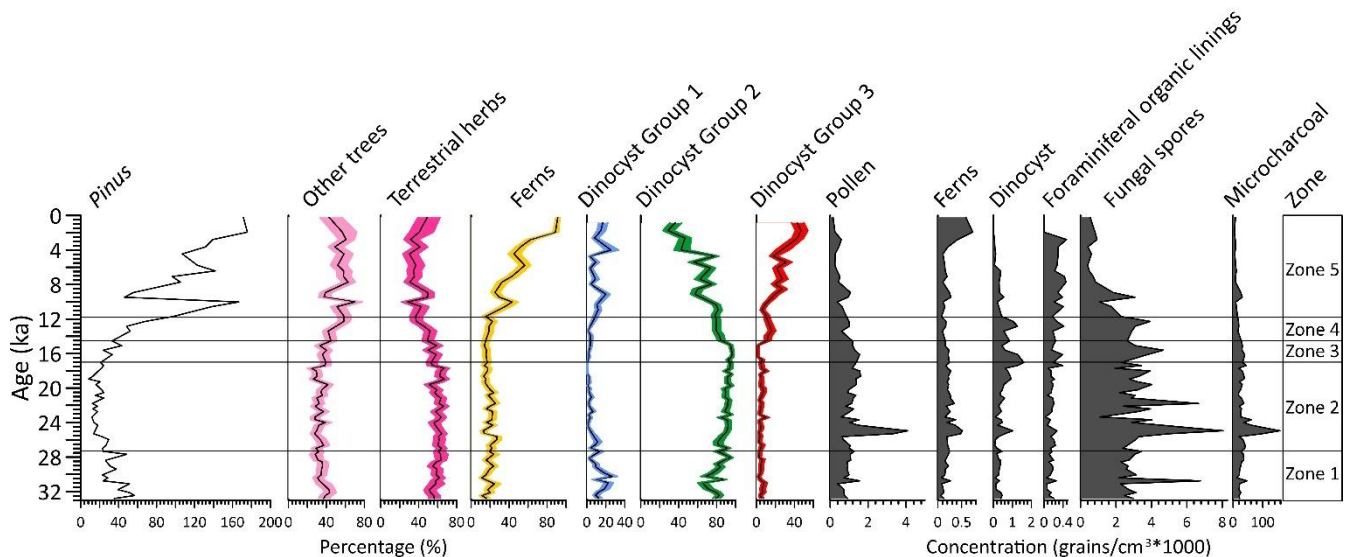
232 The $\delta^{18}\text{O}$ values of planktonic foraminifera *G. ruber* shells range from -3.2‰ to 0.3‰ (mean= -1.1‰) with higher values
233 prior to 18.7 ka, then started decreasing to much lower values with a short decline around 17.5-14.7 ka (Fig. 3g). The $\delta^{13}\text{C}$
234 values range from 0.7‰ to 2.5‰ (mean= 1.7‰) with relatively low values prior to 16 ka (Fig. 3h), there after increasing but
235 with substantial variation.

236 Mean Mg/Ca-derived SSTs range from 22.1°C to 29.7°C (mean = 24.8°C) across the core (Fig. 3i). Relatively low values
237 ($23.2\text{-}25.2^\circ\text{C}$, mean = 24.2°C) occur prior to 21.9 ka, followed by a further decline to the lowest values ($22.1\text{-}24.6^\circ\text{C}$, mean =
238 23.1°C) between 21.9-17.5 ka. After 17.5 ka, SSTs increase progressively toward the highest values observed in the record
239 ($23.5\text{-}29.7^\circ\text{C}$, mean = 26.8°C) with a short decline around 16.6-14.7 ka .

240 4.5 Palynological record

241 The complete diagrams of pollen, dinocyst percentages and concentrations, and charcoal results are shown in Figs. S2-S6.
242 Pollen concentration is variable, with particularly high concentrations ($390\text{-}4100$ grains/ cm^3 ; mean = 1200 grains/ cm^3) prior
243 to 16.1 ka, and highest concentrations around 25.3-25.0 ka ($3300\text{-}4100$ grains/ cm^3 ; mean = 3700 grains/ cm^3) (Fig. 4). Similarly,
244 charcoal exhibits the highest concentrations ($36\text{-}155 \times 10^3$ particles/ cm^3 ; mean = 83×10^3 particles/ cm^3) around 25.3-23.7 ka,
245 decreasing after 15.6 ka, reaching minimum values at the top of the core ($9\text{-}31 \times 10^3$ particles/ cm^3 ; mean = 21×10^3 particles/ cm^3)
246 (Figs. 4 and S6). Dinocyst concentrations are relatively low, ranging from $7\text{-}1600$ cysts/ cm^3 (average of 450 cysts/ cm^3) with
247 high values of $110\text{-}1600$ cysts/ cm^3 (average of 650 cysts/ cm^3) between 25.6-11.7 ka (Figs. 4 and S5). After 11.7 ka, dinocyst
248 concentrations decrease, reaching a minimum at the end of the record.

249

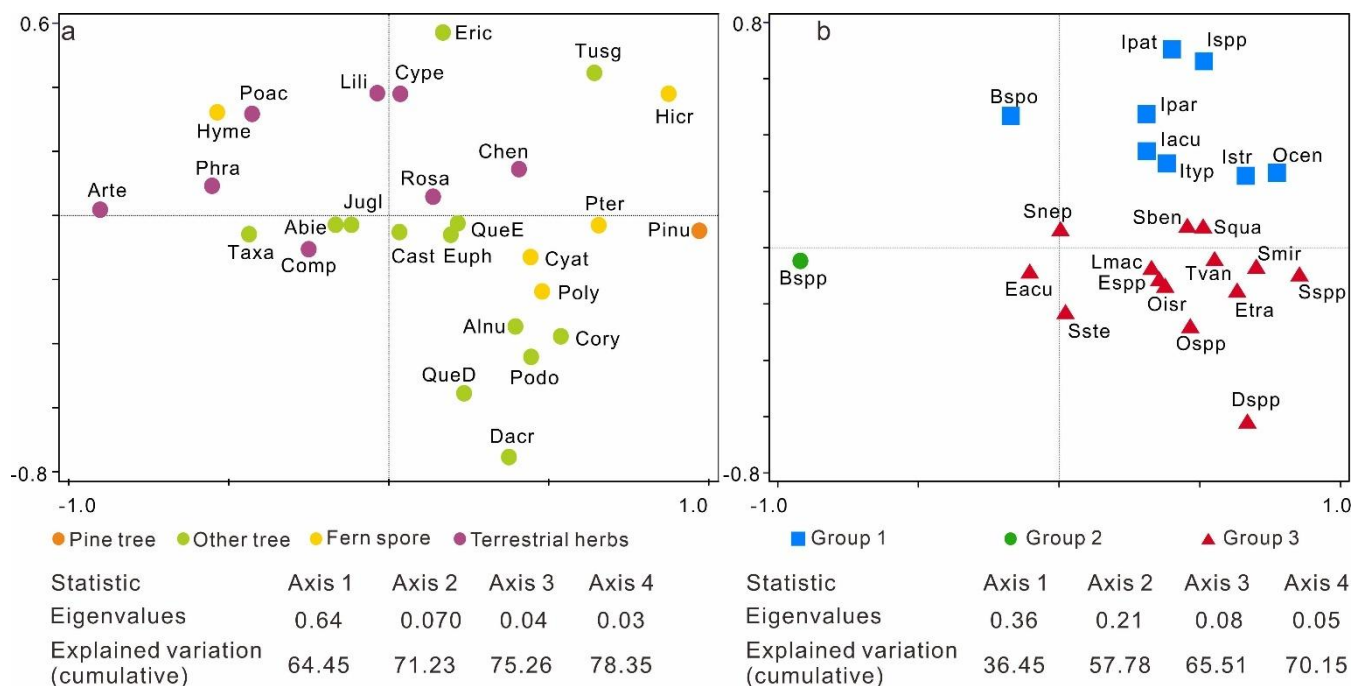


250

251 **Figure 4:** Percentages (%) of dominated pollen taxa, including pollen of *Pinus*, other trees, terrestrial herbs, fern spores, and
252 three dinocyst groups based on principal component analysis (PCA) analysis, concentrations (grains/ $\text{cm}^3 \times 1000$) of pollen, fern
253 spores, dinocyst, foraminiferal organic linings, fungal spores and microcharcoal concentration (particles/ $\text{cm}^3 \times 1000$).

254 According to the PCA results (Fig. 5a), pollen and spore taxa are well-separated based on their associated biomes. Specifically,
255 *Pinus* and fern spore (notably *Hicriopteris*, *Pteris*, Polypodiaceae and Cyathaceae) form a distinct cluster on the positive end
256 of axis 1, while characteristic terrestrial herbs (particularly *Artemisia*, Poaceae and Cyperaceae) are separated along the
257 negative end of axis 1 and relatively positive side of axis 2. Three groups of dinocyst taxa can be distinguished based on the

258 PCA results, showing clearly different trends across the record (Fig. 5b). Group 1: *Operculodinium centrocarpum*,
 259 *Impagidinium* spp., *Impagidinium aculeatum*, *Impagidinium patulum*, *Impagidinium paradoxum*, *Impagidinium striatum*,
 260 *Impagidinium* type1; *Bitectatodinium spongium*; Group 2: *Brigantedinium* spp.; Group 3: *Echinidinium* spp., *Echinidinium*
 261 *aculeatum*, *Echinidinium transparentum*, *Selenopemphix nephroides*, *Stellasinium stellatum*; *Selenopemphix quanta*,
 262 *Dubridinium* spp., *Operculodinium israelianum*; *Operculodinium* spp., *Lingulodinium machaerophorum*, *Tuberculodinium*
 263 *vancampoae*, *Spiniferites mirabilis*, *Spiniferites* spp.; *Spiniferites bentori*.



264

265 **Figure 5:** Results of the principal component analysis (PCA) illustrating the ordination of pollen (a) and dinocyst taxa (b) from
 266 core SCS GC-1 with colored symbols referring to the groups. For pollen, pine tree (orange): Pinu (*Pinus*); other tree (light
 267 green): QueE (*Quercus evergreen*), QueD (*Quercus decedious*), Alnu (*Alnus*), Podo (Podocarpaceae), Dacr (*Dacrycapus*),
 268 Taxa (Taxaceae), Abie (*Abies*), Tusg (*Tusga*), Eric (Ericaceae), Jugl (*Juglans*), Cory (*Corylus*), Cast (*Castanea*), Euph
 269 (Euphorbiaceae); fern spores (yellow): Hicr (*Hicriopteris*), Pter (*Pteris*), Cyat (Cyatheaceae), Poly (Polypodiaceae), Hyme
 270 (Hymenophyllaceae); terrestrial herbs (purple): Arte (*Artemisia*), Poac (Poaceae), Cype (Cyperaceae), Comp (Compositae),
 271 Phra (*Phragmites*), Chen (Chenopodiaceae), Rosa (Rosaceae), Lili (Liliaceae). For dinocyst groups, Group 1 (blue): Ocen (*O.*
 272 *centrocarpum*), Ispp (*Impagidinium* spp.), Iacu (*Impagidinium aculeatum*), Ipat (*Impagidinium patulum*), Ipar (*Impagidinium*
 273 *paradoxum*), Istr (*Impagidinium striatum*), Ityp (*Impagidinium* type1), Bspo (*Bitectatodinium spongium*); Group 2: Bsp
 274 (*Brigantedinium* spp.); Group 3: Esp (Echinidinium spp.), Eacu (*Echinidinium aculeatum*), Etra (*Echinidinium*
 275 *transparentum*), Snep (*Selenopemphix nephroides*), Sste (*Stellasinium stellatum*), Squa (*Selenopemphix quanta*), Dsp
 276 (*Dubridinium* spp.), Oisr (*Operculodinium israelianum*), Osp (Operculodinium spp.), Lmac (*Lingulodinium*
 277 *machaerophorum*), Tvan (*Tuberculodinium vancampoae*), Sben (*Spiniferites bentori*), Smir (*Spiniferites mirabilis*), Ssp
 278 (*Spiniferites* spp.).

279 Separate CONISS analysis were performed for pollen and dinocyst data, with results shown in Figs. S2 and S4. Considering
 280 that the zonations based on pollen and dinocyst data show very similar results, five main zones can be recognized in the record
 281 for the purpose of synthesizing the multi-proxy climatic signal (Fig. 4):

282 4.5.1 Zone 1 (301-237cm, 32.8-27.3 ka)

283 This zone is characterized by relatively high percentages of *Pinus* and evergreen *Quercus*, while pollen taxa of terrestrial herbs
284 such as *Artemisia*, Poaceae and Cyperaceae as well as fern spores including *Hicriopteris*, Polypodiaceae, Cyathaceae are
285 relatively low (Figs. 4 and S2). High fungal spore concentrations here coincide with low charcoal concentrations. The
286 percentages of heterotrophic taxa *Brigantedinium* spp. (Group 1) increase gradually to the end of this zone, whereas the
287 percentages of autotrophic taxa (Group 2) particularly *Impagidinium* species reach their maximum levels in the record but
288 decline towards the end of this phase (Figs. 4 and S4). Concentrations of foraminiferal organic linings reach minimum in this
289 zone.

290 4.5.2 Zone 2 (237-109 cm, 27.3-17.0 ka)

291 The percentage of *Pinus* pollen decreases to its lowest values of the entire record. Meanwhile, terrestrial herb taxa, particularly
292 *Artemisia*, increase to their highest levels along with fungal spores. Some fern spore types, including Polypodiaceae,
293 Hymenophyllaceae, Cyatheaceae and *Pteris*, also exhibit relatively high values compared to Zone 1 (Figs. 4 and S2).
294 Concentrations of pollen, fern spores and charcoal all reach maximum values, peaking around 25.3-24.3 ka when dinocyst
295 concentrations also exhibit a maximum, along with *Brigantedinium* spp. On the other hand, Group 1 dinocyst taxa are at
296 minimum values in this zone. Concentrations of foraminiferal organic linings remain at low value in this zone.

297 4.5.3 Zone 3 & Zone 4 (109-69 cm, 17.0-11.7 ka)

298 CONISS analysis suggests a sub-zone (zone 3) around 17.0-14.5 ka which is marked by a further decline of *Pinus* and increase
299 in herb pollen. Then zone 4 is characterized by the rapid increase in *Pinus* pollen, accompanied by a sharp decline in terrestrial
300 herbs, especially *Artemisia*. Concentrations of fungal spores exhibit a declining trend and return to the levels observed in Zone
301 1. Concentrations of pollen, fern spores and charcoal also exhibit a declining trend to reach near the lowest levels, whereas
302 dinocyst concentrations remain relatively prominent. However, the percentage of *Brigantedinium* spp. exhibits a decline in
303 this zone, accompanied by a marked increase of Group 3 taxa, including *Dubridinium* spp. and *Echinidinium* spp. Meanwhile,
304 dinocysts in Group 2 achieve relatively high values. Concentrations of foraminiferal organic linings increase gradually from
305 the beginning of this zone.

306 4.5.4 Zone 5 (69-0 cm, 11.7 ka-present)

307 The percentages of *Pinus* pollen reach their highest values of the entire record interrupted around 9.5-9.0 ka by a very marked
308 decline to values close to those of Zone 1. The abrupt reduction in *Pinus* pollen is also observed in the overall pollen, fungal
309 spore, charcoal concentration, and in terrestrial herb pollen especially. Additionally, this zone is characterized by the increase
310 in fern spores, particularly *Hicriopteris* which exhibits a short, sharp increase around 2.8 ka (Figs. 4 and S2). The percentage
311 of *Brigantedinium* spp. decreases to the lowest values of the entire record, whereas the percentage of Group 3 dinocyst taxa,
312 along with the concentration of foraminiferal organic linings all reach their highest values.

313 5. Discussion

314 5.1 Environmental significance of key proxies

315 5.1.1 K/Al and Ti/Al

316 In comparison to single elements, elemental ratios which are insensitive to dilution effects, are more useful as environmental
317 indicators (Govin et al., 2012). Ti is highly enriched in mafic and volcanic rocks, while Al is a major component of most
318 common clay mineral found in all types of weathered continental crust. The SCS is surrounded by diverse geological terrains
319 with distinct Ti/Al ratios originating from different sources such as the Luzon Volcanic Arc (Philippines), Taiwan and other

320 basaltic sources with high Ti/Al, while with low Ti/Al originating from the major continental river systems that drain ancient,
321 weathered landmasses. Thus, Ti/Al can provide a robust picture of terrestrial input and its origin in the complex environment
322 of the SCS. High Ti/Al indicates increased relative input of sediment from a volcanic or mafic source/less chemical, and low
323 Ti/Al indicates increased relative input of sediment from a felsic continental source (e.g., Pearl River, Mekong River) (Hu et
324 al., 2013; Wan et al., 2007). K/Al and Ti/Al records of ODP Site 1143 from the SCS generally show low values during glacial
325 periods and high values during interglacial periods, clearly indicating that increase in K/Al and Ti/Al is probably related to
326 wetter conditions and thus the intensified chemical weathering (Clift et al., 2008; Tian et al., 2011; Wei et al., 2004).

327 5.1.2 Source area and transport of pollen and spores

328 In the northern SCS sediments, the modern distribution of tree pollen, particularly *Pinus*, shows disproportionately high
329 representation relative to other pollen types. This suggests substantial contributions from south and southeast China,
330 transported primarily by the northeasterly winter monsoon and associated wind-driven currents. While elevated *Pinus*
331 percentages can signal either a strengthened winter monsoon or a cool, humid climate (Luo et al., 2018; Sun et al., 2003), PCA
332 results (Fig. 5a) indicate that this ambiguity can be resolved by incorporating fern spore data. Unlike wind-dispersed *Pinus*
333 pollen, the larger, heavier spores of ferns are primarily transported by river runoff. Their high abundance in sediments therefore
334 signals a proximal source from humid montane forests (e.g., in Taiwan and southern China), reflecting a humid climate
335 controlled by the EASM (Kaars et al., 2000; Sun et al., 2000b; Wang et al., 2009). Consequently, a simultaneous peak in both
336 *Pinus* pollen and fern spores is incompatible with a scenario of solely strengthened, dry winter winds. Instead, this combined
337 signal robustly indicates a cool and humid climatic regime. In this regime, a vigorous EASM delivered high rainfall, which
338 promoted fern-rich vegetation and riverine spore transport, while the EAWM remained active enough to distribute *Pinus* pollen
339 without dominating the climatic regime. Therefore, we propose a possible interpretation for the low *Pinus* during the glacial
340 period and high *Pinus* during the interglacial period: during the glacial period especially during the LGM, a strong but dry
341 EAWM could efficiently transported *Pinus* pollen from distant montane source areas. However, local arid conditions on the
342 exposed continental shelf limited the growth of conifers near the core site leading to moderate percentages in the record; during
343 the interglacial period especially during the Holocene, despite the increased distance due to sea-level rise, enhanced EASM-
344 driven humidity favoured the expansion of Pine forests in source regions. Concurrently, altered atmospheric and oceanic
345 circulation patterns likely facilitated the long-distance transport of pollen to the deep basin.

346 *Artemisia*, Poaceae and Cyperaceae pollen are the main components of terrestrial herbs observed in the core. *Artemisia* spp. is
347 currently widely distributed in temperate grassland and steppe which is associated with cool, semi-arid conditions (Bandara et
348 al., 2023; Sun et al., 2003). Although Poaceae and Cyperaceae pollen indicate a range of different habitats, high percentages
349 of Poaceae pollen in the sediment are suggestive of grassland vegetation, and a high representation of Cyperaceae pollen can
350 point to wetland environments, though in association with *Artemisia* and Poaceae, it may also form part of dry grassland
351 communities (Sun et al., 2003; Wang et al., 2009).

352 Previous studies have found clear temporal variations in pollen assemblages in the SCS characterized by marked higher pollen
353 concentrations in glacial sediments than in interglacial sediments (Jiwarungrueangkul and Liu, 2021; Sun et al., 2000a; Sun
354 and Luo, 2001; Sun et al., 2003; Zheng and Lei, 1999). On one hand, the large amount of pollen in glacial sediments at the site
355 might be transported by a strengthened northeast winter monsoon from the Asian mainland and Taiwan Island. In contrast,
356 during the last glacial low stand, sea level was 120-150 m lower than today, exposing much of the northern SCS continental
357 shelf and increasing land area by roughly 24×10^4 km² (Chen et al., 2020; Sun et al., 2000a; Wang et al., 2009). The northern
358 SCS would likely receive substantial pollen and spore amounts via wind or water from the exposed continental shelf which
359 was covered by grassland under the prevailing dry and temperate climate of the time (Luo and Sun, 2005; Sun et al., 2003).
360 This expansion of open, terrestrial herb-dominated vegetation likely occurred on both the exposed shelf and the adjacent
361 continental catchments due to the overall drier glacial climate. Typically, during glacial periods, herbaceous vegetation is
362 predominant in the region, whereas during interglacial periods tree and ferns dominate the terrestrial land mass adjacent to the
363 SCS (Sun et al., 2000a; Sun and Luo, 2001). Such glacial-interglacial transitions are driven by changes in climate, or ocean
364 currents, or both. During MIS 2 (21-11.5 ka), *Artemisia* increased again and occupied most of the extensive emerged
365 continental shelf (Sun et al., 2003). Accordingly, the ratio of trees/herbs pollen is a valuable indicator of glacial-interglacial
366 cycles along with their associated vegetation and climate conditions.

367 5.1.3 Dinocysts

368 Although modern dinocyst distributions are strongly correlated with sea surface conditions such as sea surface temperature,
369 sea surface salinity, nutrient levels and productivity (Dale, 1996; Marret and Zonneveld, 2003; Zonneveld et al., 2024),
370 dinocyst deposition and preservation in marine sediments are affected by various non-ecological, taphonomic factors which
371 may alter the primary dinocyst accumulation in the sediment (Holzwarth et al., 2007). It is therefore crucial to account for
372 these factors before relating the fossil dinocyst record to palaeoenvironmental conditions. Upwelling off west Luzon is driven
373 by the EAWM and intensifies during stronger EAWM phases. This process brings nutrient-rich subsurface waters to the surface,
374 promoting enhanced dinoflagellate production (Yuan et al., 2004). The Kuroshio Current, which transports warm and high-
375 salinity water into the northern SCS leading to a significant increase in sea surface temperature, is also a significant factor
376 influencing dinoflagellate growth. Additionally, heterotrophic taxa, such as degradation-sensitive species from the
377 *Protoperidinium* genus, are more susceptible to aerobic degradation compared to autotrophic taxa (Holzwarth et al., 2007).
378 This may be influenced by the water oxygen content which may therefore alter dinocyst assemblages before and after
379 sedimentation (Zonneveld et al., 2008). However, the persistent dominance of heterotrophic dinocysts in the record (up to 99%
380 with mean values of 85%) suggests that selective dissolution of protoperidiniacean species relative to other taxa in the
381 sediments is negligible (Zhao et al., 2017).

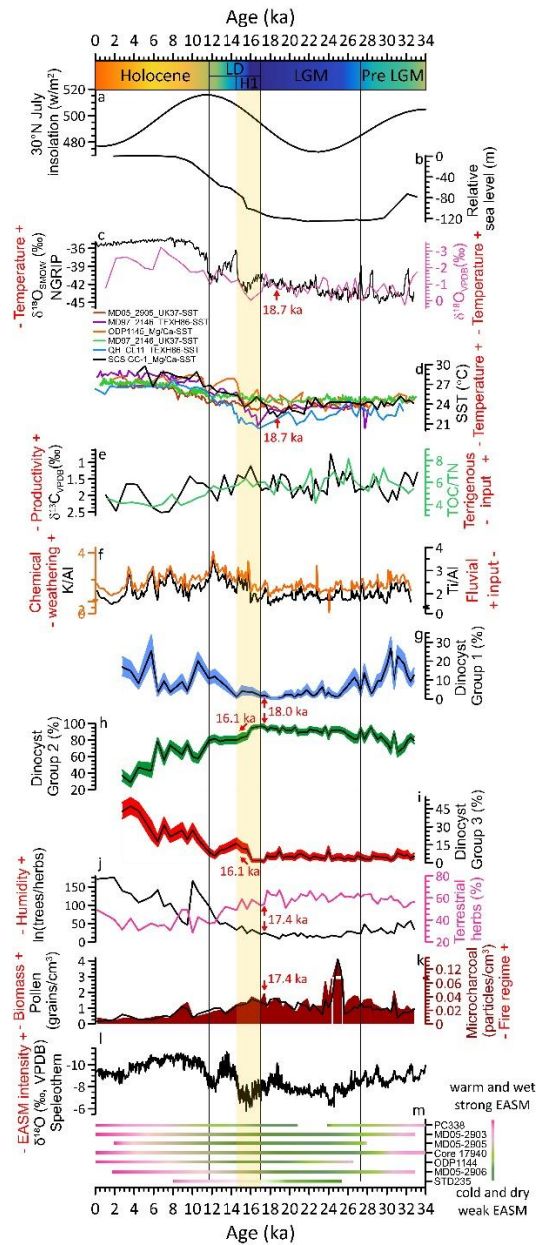
382 *Impagidinium* cysts as well as *O. centrocarpum* typically indicate open ocean, fully marine settings characterized by low
383 primary productivity, low nutrient levels, and well-oxygenated bottom waters (Zonneveld et al., 2013; Zonneveld and
384 Pospelova, 2015). Modern surface dinocyst distribution in SCS shows that most of *Impagidinium* species, *Nematosphaeropsis*
385 *labyrinthus* and *Polysphaeridium zoharyi* are positively correlated with water depth. Their highest abundances were observed
386 in the northern slope-deep basin which is influenced by the Kuroshio Current, indicating an open-ocean environment (Li et al.,
387 2020). In the northern Philippine Sea, the predominance of *Impagidinium* taxa from the bottom sediments is also indicative of
388 pelagic and tropical regions (Matsuoka, 1981). During winter, the Kuroshio Current transports high-salinity, low-nutrient
389 waters from the Philippine Sea through the Luzon Strait, which then flows along the continental shelf break, reaching the study
390 area in the northern SCS. This provides further evidence that the increased abundance of Group 1 taxa may reflect typical
391 nutrient-poor open ocean environments and enhanced influence of the Kuroshio Current. Dinocysts preserved in SCS GC-1
392 are dominated by *Brigantedinium* spp. (28-96%, mean = 80%), which have also been observed from sediment trap samples in
393 the southwest Taiwan waters of the SCS with high representation ranging from 68% to 91% (Li et al., 2018b). High abundances
394 of *Brigantedinium* spp. are characteristic of increased nutrient supply (Dale, 1996), which has been used as an indicator of
395 primary productivity (Li et al., 2020; Zonneveld et al., 2013). In addition, *Brigantedinium* spp. is usually more abundant near
396 the winter upwelling zone in the South China Sea (Li et al., 2020). Therefore, Group 2 taxa, characterized by the dominance
397 of *Brigantedinium* spp., indicates intensified upwelling conditions with strong terrigenous influence that contrasts with open-
398 ocean oligotrophic conditions indicated by Group 1. The stratigraphic variation of Group 2 cysts (Fig. 6h) displays an inverse
399 relationship with Mg/Ca-SST, supporting the glacial 'high-productivity/low-temperature' paradigm. Group 3 taxa,
400 characterized by dinocysts such as *Echinidinium* spp. and *S. quanta* are typically adapted to fully marine, eutrophic, and highly
401 productive regimes, and are likely indicative of water column stratification and upwelling processes in open ocean
402 environments (Zonneveld et al., 2013). The shift from Group 2 to Group 3 dominance during the deglaciation may thus signal
403 a transition from terrestrial nutrient-driven productivity to a more stratified, marine-dominated productivity regime.

404 5.2 Shelf exposure, aridity and high marine productivity during the LGM

405 Over the past 33 ka, four distinct climatic phases have been clearly recognized based on our multi-proxy record (Fig. 6): pre-
406 LGM (32.8-27.3 ka), LGM (27.3-17.0 ka), last deglaciation (17.0-11.7 ka) which includes the Heinrich Stadial 1 (H1, 17.0-
407 14.5 ka), and the Holocene (11.7 ka-present). This sequence reveals a pronounced glacial-interglacial transition. The pre-LGM
408 phase already exhibited features of a cooler and drier glacial regime, which became more pronounced during the LGM. This
409 period was characterized by markedly higher sedimentation rates (Fig. 3a), cooler SST (Figs. 6c and 6d), higher primary
410 productivity (Figs. 6e and 6h), reduced humidity (Figs. 6f, 6j, 6l and 6m), a landscape dominated by herbaceous vegetation
411 (Fig. 6j), and strengthened fire activity (Fig. 6k).

412 During the LGM, sea levels were approximately 120 m lower than present, leading to extensive exposure of the northern SCS
413 continental shelf (Fig. 6b), which effectively extended the coastal plains and created an expansive, low-relief terrestrial surface
414 (Hanebuth et al., 2000). While previous studies have attributed elevated charcoal and pollen concentrations during the LGM
415 to the reduced distance to sediment sources from this exposed continental shelf (Luo and Sun, 2005; Sun et al., 2000a), our
416 multi-proxy data support this proximal-source effect and further demonstrate that the vegetation colonizing the shelf was
417 fundamentally shaped by the cold and dry glacial climate. Specifically, the high percentages of terrestrial herb pollen, in
418 particular arid-tolerant *Artemisia* together with Poaceae and Cyperaceae, minimum tree pollen (Fig. S2), and trees/herbs ratio
419 (Fig. 6j) all indicate a herbaceous landscape. Moreover, independent climate proxies also confirm the arid conditions: the low
420 K/Al ratio (Fig. 6f) suggesting reduced chemical weathering under drier conditions, aligns with the enriched speleothem $\delta^{18}\text{O}$
421 values indicating a weakened EASM and reduced rainfall over the region (Fig. 6l) (Cheng et al., 2016). This aridity suppressed
422 forest growth and favoured drought-tolerant herbs. Concurrently, the maximal concentrations of microcharcoal (Fig. 6k),
423 especially the large charcoal particles ($>100\ \mu\text{m}$) indicative of local fires (Fig. S6), coincide with maximal herb pollen. This is
424 ecologically explainable: herbaceous vegetation especially in dry seasonal climate could produce fine, highly flammable fuel
425 that supports frequent and potentially high-intensity fires. Therefore, the high terrestrial herb pollen percentage reflects a dual
426 control: the exposed shelf provided a vast proximal source area, while the glacial climate determined that this area and possibly
427 the adjacent continental catchments would be occupied by drought-adapted grassland/steppe vegetation.

428 The substantially shortened distance between the exposed shelf and the core site (Lambeck et al., 2014) would have facilitated
429 more efficient transfer of terrigenous nutrients to proximal deep-sea areas. The low Ti/Al ratios (Fig. 6f) suggest that this
430 enhanced input originated mainly from felsic continental rivers (e.g., the Pearl River). Although weakened EASM would
431 typically suppress fluvial discharge, this effect appears to have been offset by the closer coastline and the likely persistence of
432 eolian dust transport from the arid Chinese mainland. Concurrently, this open landscape, combined with likely enhanced
433 erosion under such variable glacial conditions would have supplied abundant terrestrial nutrients to the adjacent ocean.
434 Enhanced terrigenous nutrient delivery from this expansive, herb-covered continental shelf and arid continental hinterlands
435 also appears to have stimulated elevated marine productivity during the LGM. This is clearly recorded in our marine proxies:
436 TOC/TN ratio with a range between 3.8-8.1 throughout the record indicates a marine phytoplankton-dominated organic matter
437 source (Meyers, 1999), while elevated $\delta^{13}\text{C}$ values of planktonic foraminifera (Fig. 6e) during this period suggest enhanced
438 organic carbon export. Critically, the combined fluvial and eolian nutrient fluxes would have created a nutrient-replete surface
439 ocean, directly favouring heterotrophic dinoflagellates such as *Brigantedinium* (Smayda and Trainer, 2010). This can thereby
440 well explain the dinocyst record characterized by pronounced dominance of dinocyst Group 2 (*Brigantedinium* spp. which can
441 constitute up to 97%, mean = 81%) indicative of high nutrient availability, alongside the near-absence of oligotrophic, open-
442 ocean Group 1 (Figs. 6g and 6h), points to a productivity regime sustained by abundant terrestrial nutrient supply rather than
443 open-ocean processes. This pattern is consistent with global compilations showing that organic carbon accumulation rates
444 during glacial maxima were $\sim 50\%$ higher than interglacial intervals (Cartapanis et al., 2016). Independent evidence from the
445 northern SCS similarly links higher glacial productivity to intensified winter monsoon winds, enhanced water-column mixing,
446 upwelling, and increased land-derived nutrient supply (Li et al., 2008). Our dinocyst record, characterized by the dominance
447 of a heterotrophic, highly nutrient-dependent taxon, strongly supports the interpretation that terrestrial nutrient supply was a
448 key mechanism together with the complementation of the physical forcing of strengthened winter monsoon-driven mixing.



449

450 **Figure 6:** 30°N July insolation (Laskar et al., 2004) (a); relative sea level on the Sunda Shelf, South China Sea (Hanebuth et
 451 al., 2000) (b); NGRIP $\delta^{18}\text{O}_{\text{SMOW}}$ (Andersen et al., 2004) (c, black) and stable oxygen $\delta^{18}\text{O}_{\text{VPDB}}$ of planktonic foraminifera from
 452 SCS GC-1 (c, pink); SST records from MD052905 (Zhou et al., 2012), MD972146 (Lin et al., 2014), ODP1145 (Oppo and
 453 Sun, 2005), QHCL11 (Liu et al., 2020) and SCS GC-1 (d); stable carbon $\delta^{13}\text{C}_{\text{VPDB}}$ of planktonic foraminifera (e, black) and
 454 TOC/TN ratio (e, green); major element ratio Ti/Al (f, black) and K/Al (f, orange), percentages of three dinocyst groups (g, h,
 455 i); ratio of trees/herbs (j, black) and percentages of terrestrial herbs (j, pink); pollen concentration (k, black) and microcharcoal
 456 concentration (k, dark red shading); compilation of speleothem $\delta^{18}\text{O}_{\text{VPDB}}$ values from central China (l) (Cheng et al., 2016);
 457 summary of records indicating climate and potential intensity of EASM (m) (Sun et al., 2000a; Sun et al., 2000b; Luo and Sun,
 458 2005; Zhou et al., 2012; Xie et al., 2014; Dai and Weng, 2015; Dai et al., 2015a; Yu et al., 2017; Li et al., 2019). Pre LGM:

459 pre Last Glacial Maximum; LGM: Last Glacial Maximum; LD: last deglaciation; H1: Heinrich Stadial 1. Red arrows indicate
460 the onset of the transition in different proxies.

461 **5.3 Early ocean warming, monsoon intensification and ecosystem response since the last deglaciation**

462 Since the last deglaciation, the northern SCS has experienced a comprehensive environmental transformation characterized by
463 decreasing sedimentation rates, rising SST, declining primary productivity, increased moisture availability, a pronounced
464 expansion of pine forests, and reduced fire activity. Critically, our record reveals that the initial signal of this transformation
465 was an SST increase at ca. 18.7 ka (Figs. 6c and 6d) (Andersen et al., 2004; Lin et al., 2014; Liu et al., 2020; Oppo and Sun,
466 2005; Zhou et al., 2012), which began ~1.3 ka earlier than the major shifts in terrestrial vegetation and other sediment proxies
467 (ca. 17.4 ka, Figs. 6j and 6k). This early ocean warming provides direct, local evidence for the primacy of ocean-atmosphere
468 forcing in initiating the regional deglacial transition. Additionally, the millennial-scale event of H1 (17.0-14.5 ka) is embedded
469 within the early phase of this warming, recorded as an interval of low SST, high $\delta^{18}\text{O}_{\text{VPDB}}$ of planktonic foraminifera and high
470 percentages of terrestrial herb pollen. This suggests that short-period cold and dry conditions linked to North Atlantic forcing
471 temporarily modulated but did not override the underlying tropical warming trend in the study area (Clark et al., 2012).

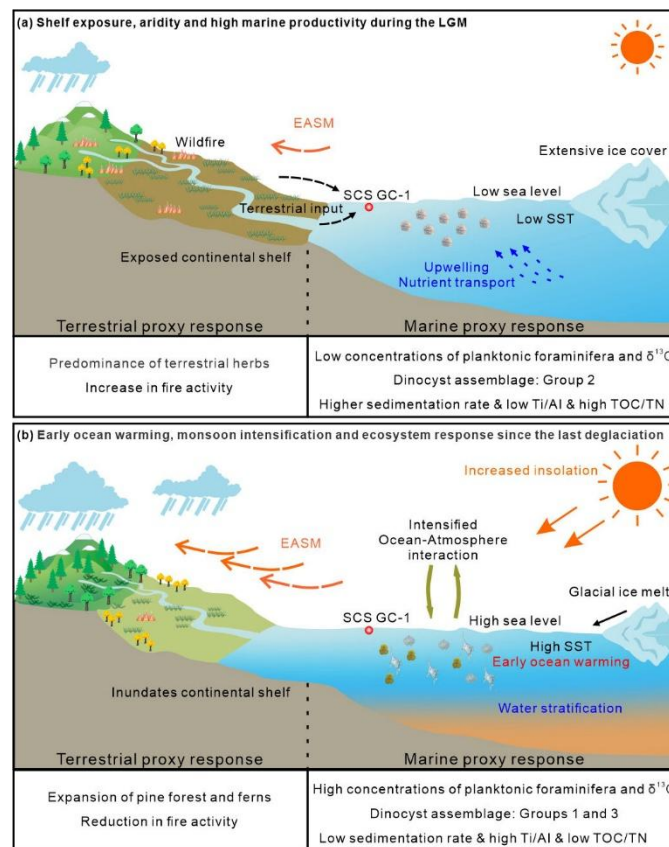
472 The earlier onset of SST warming corresponds more closely with rising boreal summer insolation (Fig. 6a) (Laskar et al., 2004)
473 than with the rate of sea-level rise (Fig. 6b) (Hanebuth et al., 2000). This implies that tropical ocean warming, likely amplified
474 by ocean-atmosphere feedbacks, acted as the initial trigger for subsequent environmental changes. This effect is especially
475 pronounced in the tropics and is consistent with the concept of tropical ocean-atmosphere forcing (Cheng et al., 2019; Xie et
476 al., 2010). For instance, seminal work has shown that the timing of peak East Asian Monsoon intensity differs between marine
477 and terrestrial records (An et al., 2000). Furthermore, while terrestrial pollen records from East Asian indicate rapid warming
478 around 15 ka, synchronous with Greenland ice core and stalagmite records from southern China, marine SST reconstructions
479 (based on Mg/Ca-SST and long chain alkenone U^k_{37} -SST) from the same record indicate that SSTs began to rise as early as
480 20-19 ka, a trend more consistent with the early warming of the Western Pacific Warm Pool (Xu et al., 2013). This 3-4 kyr lag
481 of terrestrial warming behind western Pacific oceanic warming highlights the differential thermal response and reinforces the
482 interpretation that early ocean warming served as a critical forcing mechanism.

483 The sequence of multi-proxy changes in our record reveals a clear mechanistic chain initiated by this early SST rise. The first
484 detectable response in our marine proxies is a shift in dinocyst assemblages at ca. 18.0 ka, marked by the incipient increase of
485 oligotrophic Group 1 dinocysts and the onset of decline in the highly nutrient-dependent Group 2 dinocysts. We attribute this
486 to a direct oceanographic response to warming: enhanced upper water column stratification reduced vertical nutrient supply,
487 favoring oligotrophic taxa over heterotrophic ones. Subsequent to this initial marine response, the physical reconfiguration of
488 the coastline due to sea level rise further modulated the environmental trajectory. The inundation of the exposed continental
489 shelf increased the distance from terrestrial sediment sources to the core site (Luo and Sun, 2005; Sun et al., 2000a) and created
490 a sediment trap on the newly formed shallow marine environments, leading to a dramatic reduction in terrigenous material
491 reaching our deep basin site (Liu et al., 2003; Wang and Sun, 1994). This is reflected in markedly lower sedimentation rates
492 and increased Ti/Al ratios (Figs. 3a and 6f), indicating reduced terrestrial input. The combination of sustained ocean warming
493 and reduced nutrient supply further suppressed heterotrophic dinoflagellates such as *Brigantedinium* (Smayda and Trainer,
494 2010), driving a pronounced decline in Group 2 dinocysts from 16.1 ka and a concurrent increase in Group 3 dinocysts which
495 is indicative of more stratified, marine-dominated conditions (Figs. 6h and 6i), coincident with a reduction in TOC/TN (Fig.
496 6e). This shift marks a fundamental transition in the productivity regime: from a terrigenous nutrient-driven regime (Group 2
497 dominated during the LGM) to a more stratified, marine-dominated regime (Group 3).

498 Parallel to these oceanic changes, the shrinking continental shelf also constrained the habitat for herbaceous vegetation.
499 Concurrently, the intensification of the EASM, a large-scale atmospheric response like initiated and reinforced by the warming
500 tropical ocean and the evolving land-sea thermal contrast, is recorded by the rapid negative shift in the speleothem $\delta^{18}\text{O}$ records
501 (Fig. 6l) (Cheng et al., 2016) and supported by multiple palaeorecords from the northern SCS (Fig. 6m) (Dai and Weng, 2015;
502 Dai et al., 2015; Li et al., 2019; Luo et al., 2015; Sun et al., 2000a; Sun et al., 2000b; Xie et al., 2014; Yu et al., 2017; Zhou et
503 al., 2012). This strengthened monsoon brought increased moisture to the region, supporting the expansion of pine forests and
504 ferns (Figs. 4 and 6j) and leading to a sharp reduction in fire activity, as evidenced by decreased charcoal concentrations (Fig.
505 6k).

506 Additional evidence supports this ecosystem-scale reorganization. Relatively high concentrations of foraminiferal organic
 507 linings (Fig. 4) indicate that water depth and open ocean environments had become suitable for planktonic foraminifera
 508 (Tyszka et al., 2021), while the decline in coprophilous fungal spores suggests an ecosystem-level response in herbivore
 509 populations to the changing landscape (Fig. 4) (Lee et al., 2022). Similar patterns with increased fern spores, decreased
 510 terrestrial herbs and reduced dinocyst concentrations were also recorded from 12.5-6.8 ka in the core GLW31D from the
 511 northern SCS (Li et al., 2017). Additionally, periodic peaks in oligotrophic, open-ocean dinocyst Group 1, particularly around
 512 10.6 ka and 5.8 ka (Fig. 6g), point to short enhancements of the warm, nutrient-poor Kuroshio Current intrusion (Liu et al.,
 513 2016b), which would further suppressed productivity in the northern SCS. Independent evidence for strengthened Kuroshio
 514 intrusion during the early Holocene is also recorded in core GLW31D from the northern SCS (Li et al., 2021).

515 Collectively, our multi-proxy dataset demonstrates that the deglacial environmental transition in the northern SCS reflects the
 516 complex interplay of multiple forcings (Fig. 7). The sequence began with tropical ocean warming, evidenced by the early rise
 517 in SST, which initiated the deglacial transition. This warming directly altered marine conditions (stratification, productivity)
 518 and, throughout ocean-atmospheric interactions, helped trigger the intensification of the EASM. These primary changes were
 519 then amplified and modulated by the physical effects of sea-level rise (altered sediment transport and coastal geography). This
 520 multi-mechanism framework highlights the northern SCS as a sensitive region where the coherent yet time-transgressive
 521 responses of marine and terrestrial systems to global climatic changes are clearly recorded during the last deglaciation.



522

523 **Figure 7:** A conceptual framework of driving mechanisms and associated environmental responses during the LGM (a) and
 524 since the last deglaciation (b) based on multi-proxy record from the core SCS GC-1 in the northern SCS.

525 **6 Conclusions**

526 Our multi-proxy reconstruction from the northern SCS provides a high-resolution record of clear glacial-interglacial climatic
527 and oceanic transitions over the past 33 ka. Four distinct climatic phases are identified, viz. the pre-Last Glacial Maximum
528 (32.8-27.3 ka), Last Glacial Maximum (27.3-17.0 ka), last deglaciation (including the Heinrich Stadial 1) (17.0-11.7 ka) and
529 the Holocene (11.7 ka-present). The glacial intervals (pre-LGM and LGM) were characterized by higher sedimentation rates,
530 cooler SST, higher primary productivity, herb-dominated landscapes, reduced humidity and intensified fire activity. This
531 regime was primarily shaped by the effects of glacial low sea-level stand and arid climatic conditions, which together promoted
532 the expansion of open vegetation and enhanced the supply of terrestrial nutrients, thereby stimulating marine productivity. A
533 fundamental regime shift occurred during the last deglaciation, marked by evidently decreasing sedimentation rates, rising
534 SST, declining primary productivity, a pronounced expansion of pine forests, increased moisture availability, and diminished
535 fire activity. The early onset of SST warming (1.3 ka ahead of terrestrial shifts), points to tropical ocean-atmospheric
536 interactions as the initial trigger for the deglacial transition. The Holocene was characterized by a period of relative stability,
537 defined by the lowest sedimentation rates, warmest SST, highest humidity, maximum pine forest coverage and minimal fire
538 disturbance. In summary, the combined evidence reveals that the environmental changes of the northern SCS since the last
539 glacial period reflects a shift in the dominant climate forcing mechanisms. During the glacial period, the system was governed
540 by the combined forcing of low sea level and continental aridity, which amplified land-sea interactions and maintained high
541 marine productivity. Since the last deglaciation, the climate dynamics have transitioned to a regime where low-latitude
542 processes, initiated by early ocean warming and subsequent ocean-atmosphere coupling, became the primary driver, leading
543 to monsoon intensification and thereafter ecosystem reorganization. This study highlights the value of integrated land-sea
544 proxies in deciphering complex climate interactions and underscores the northern SCS's sensitivity to both high- and low-
545 latitude forcing. Future research employing a spatial network of cores across the SCS will be crucial to better resolve the spatial
546 patterns and teleconnections of these changes.

547 **Author Contributions**

548 Xueqin Zhao: Conceptualization, Data curation, Formal analysis, Funding acquisition, Investigation, Methodology, Project
549 administration, Supervision, Validation, Writing – original draft, Writing – review and editing; Shengjie Ye: Investigation,
550 Visualization, Writing – review and editing; Jiahui Yao: Investigation, Formal analysis, Writing – review and editing; Michael
551 Meadows: Validation, Writing – review and editing; Chengyu Weng: Validation, Writing – review and editing; Yasong Wang:
552 Visualization, Writing – review and editing; Mingxing Zhang: Investigation; Yunping Xu: Conceptualization, Writing – review
553 and editing.

554 **Competing Interests**

555 The authors declare that they have no conflict of interest.

556 **Acknowledgments**

557 This work was supported by the National Natural Science Foundation of China (42206048). We would like to thank the captain,
558 crew and especially all scientists of the R/V Songhang (Shanghai Ocean University) cruise for recovering the samples. Thank
559 Xiaodi Lu and Yinwei Xi for the sampling and helping to measure XRF. Thank Xiaodi Lu for the assistance with lab analysis.
560 Mike E. Meadows acknowledges financial support from the Jiangsu Provincial Government Overseas Talent 100 Plan,
561 SBX2021010183.

562 Data Availability

563 Data used in this study has been stored in the Pangaea database (<https://www.pangaea.de>) with specific DOI:
564 <https://doi.pangaea.de/10.1594/PANGAEA.987882> for pollen and spore , <https://doi.pangaea.de/10.1594/PANGAEA.987861>
565 for organic-walled dinoflagellate cyst, <https://doi.pangaea.de/10.1594/PANGAEA.987870> for microcharcoal,
566 <https://doi.pangaea.de/10.1594/PANGAEA.989845> for organic carbon and nitrogen content,
567 <https://doi.pangaea.de/10.1594/PANGAEA.989928> for foraminifera stable carbon and oxygen isotopes, and
568 <https://doi.pangaea.de/10.1594/PANGAEA.989846> for X-ray fluorescence (XRF) scanning data.

569 References

- 570 Aleman, J. C., Blarquez, O., Bentaleb, I., Bonté, P., Brossier, B., Carcaillet, C., Gond, V., Gourlet - Fleury, S., Kpolita, A.,
571 Lefèvre, I., Oslisly, R., Power, M. J., Yongo, O. D., Bremond, L., and Favier, C.: Tracking land-cover changes with
572 sedimentary charcoal in the Afrotropics. *Holocene*, 23, 1853-1862, doi: 10.1177/0959683613508159, 2013.
- 573 An, Z.: The history and variability of the East Asian paleomonsoon climate. *Quat. Sci. Rev.*, 19(1), 171-187, doi: S0277-
574 3791(99)00060-8, 2000.
- 575 An, Z., Porter, S. C., Kutzbach, J. E., Xihao, W., Suming, W., Xiaodong, L., Xiaoqiang, L., and Weijian, Z.: Asynchronous
576 Holocene optimum of the East Asian monsoon. *Quat. Sci. Rev.*, 19(8), 743-762, doi: 10.1016/S0277-3791(99)00031-1,
577 2000.
- 578 Andersen, K. K., Azuma, N., Barnola, J. M., Bigler, M., Biscaye, P., Caillon, N., Chappellaz, J., Clausen, H. B., Dahl-Jensen,
579 D., Fischer, H., Flückiger, J., Fritzsche, D., Fujii, Y., Goto-Azuma, K., Grønbold, K., Gundestrup, N. S., Hansson, M.,
580 Huber, C., Hvidberg, C. S., Johnsen, S. J., Jonsell, U., Jouzel, J., Kipfstuhl, S., Landais, A., Leuenberger, M., Lorrain, R.,
581 Masson-Delmotte, V., Miller, H., Motoyama, H., Narita, H., Popp, T., Rasmussen, S. O., Raynaud, D., Rothlisberger, R.,
582 Ruth, U., Samyn, D., Schwander, J., Shoji, H., Siggard-Andersen, M. L., Steffensen, J. P., Stocker, T., Sveinbjörnsdóttir,
583 A. E., Svensson, A., Takata, M., Tison, J. L., Thorsteinsson, T., Watanabe, O., Wilhelms, F., White, J. W. C., and North
584 Greenland Ice Core Project, m.: High-resolution record of Northern Hemisphere climate extending into the last
585 interglacial period. *Nature*, 431(7005), 147-151, doi: 10.1038/nature02805, 2004.
- 586 Bandara, G., Luo, C. X., Chen, C. X., Xiang, R., Herath, D. B., Yang, Z. J., and Thilakanayaka, V.: Sedimental pollen records
587 in the northern South China Sea and their paleoenvironmental significance. *J. Asian Earth Sci.*, 241, Article 105457, doi:
588 10.1016/j.jseaes.2022.105457, 2023.
- 589 Barker, S., Greaves, M., and Elderfield, H.: A study of cleaning procedures used for foraminiferal Mg/Ca paleothermometry.
590 *Geochem. Geophys. Geosyst.*, 4(9), doi: 10.1029/2003GC000559, 2003.
- 591 Blaauw, M., and Christen, J. A.: Flexible paleoclimate age-depth models using an autoregressive gamma process. *Bayesian*
592 *Anal.*, 6(3), 457-474, 418, doi: 10.1214/11-BA618, 2011.
- 593 Cartapanis, O., Bianchi, D., Jaccard, S. L., and Galbraith, E. D.: Global pulses of organic carbon burial in deep-sea sediments
594 during glacial maxima. *Nat. Commun.*, 7(1), 10796, doi: 10.1038/ncomms10796, 2016.
- 595 Chao, S., Shaw, P., and Wang, J.: Wind relaxation as possible cause of the South China Sea Warm Current. *J. Oceanogr.*,
596 51(1), 111-132, doi: 10.1007/BF02235940, 1995.
- 597 Chen, C. A., and Huang, M.: A mid-depth front separating the South China Sea water and the Philippine sea water. *J. Oceanogr.*,
598 52(1), 17-25, doi: 10.1007/BF02236530, 1996.
- 599 Cheng, H., Edwards, R. L., Sinha, A., Spötl, C., Yi, L., Chen, S., Kelly, M., Kathayat, G., Wang, X., Li, X., Kong, X., Wang,
600 Y., Ning, Y., and Zhang, H.: The Asian monsoon over the past 640,000 years and ice age terminations. *Nature*, 534(7609),
601 640-646, doi: 10.1038/nature18591, 2016.
- 602 Chen, Y., Huang, E., Schefuß, E., Mohtadi, M., Steinke, S., Liu, J., Martínez-Méndez, G., and Tian, J.: Wetland expansion on
603 the continental shelf of the northern South China Sea during deglacial sea level rise. *Quat. Sci. Rev.*, 231, 106202, doi:
604 10.1016/j.quascirev.2020.106202, 2020.
- 605 Cheng, L., Abraham, J., Hausfather, Z., and Trenberth, K. E.: How fast are the oceans warming? *Science*, 363(6423), 128-129,
606 doi: 10.1126/science.aav7619, 2019.

607 Cheng, Z., Wu, J., Luo, C., Liu, Z., Huang, E., Zhao, H., Dai, L., and Weng, C.: Coexistence of savanna and rainforest on the
608 ice-age Sunda Shelf revealed by pollen records from southern South China Sea. *Quat. Sci. Rev.*, 301, 107947, doi:
609 10.1016/j.quascirev.2022.107947, 2023.

610 Clark, P. U., Shakun, J. D., Baker, P. A., Bartlein, P. J., Brewer, S., Brook, E., Carlson, A. E., Cheng, H., Kaufman, D. S., Liu,
611 Z., Marchitto, T. M., Mix, A. C., Morrill, C., Otto-Bliesner, B. L., Pahnke, K., Russell, J. M., Whitlock, C., Adkins, J. F.,
612 Blois, J. L., Clark, J., Colman, S. M., Curry, W. B., Flower, B. P., He, F., Johnson, T. C., Lynch-Stieglitz, J., Markgraf,
613 V., McManus, J., Mitrovica, J. X., Moreno, P. I., and Williams, J. W.: Global climate evolution during the last deglaciation.
614 *Proc. Natl. Acad. Sci. U. S. A.*, 109(19), E1134-E1142, doi:10.1073/pnas.1116619109, 2012. Clift, P. D., Hodges, K. V.,
615 Heslop, D., Hannigan, R., Van Long, H., and Calves, G.: Correlation of Himalayan exhumation rates and Asian monsoon
616 intensity. *Nat. Geosci.*, 1(12), 875-880, doi: 10.1038/ngeo351, 2008.

617 Conedera, M., Tinner, W., Neff, C., Meurer, M., Dickens, A. F., and Krebs, P.: Reconstructing past fire regimes: methods,
618 applications, and relevance to fire management and conservation. *Quat. Sci. Rev.*, 28(5), 555-576, doi:
619 10.1016/j.quascirev.2008.11.005, 2009.

620 Dai, L., and Weng, C.: A survey on pollen dispersal in the western Pacific Ocean and its paleoclimatological significance as a
621 proxy for variation of the Asian winter monsoon. *Sci. China Earth Sci*, 54(2), 249-258, doi: 10.1007/s11430-010-4027-
622 7, 2011.

623 Dai, L., and Weng, C.: Marine palynological record for tropical climate variations since the late last glacial maximum in the
624 northern South China Sea. *Deep-Sea. Res. Pt II*, 122, 153-162, doi: 10.1016/j.dsr2.2015.06.011, 2015.

625 Dai, L., Weng, C., and Mao, L.: Patterns of vegetation and climate change in the northern South China Sea during the last
626 glaciation inferred from marine palynological records. *Palaeogeogr., Palaeoclimatol., Palaeoecol.*, 440, 249-258, doi:
627 10.1016/j.palaeo.2015.08.041, 2015.

628 Dale, B.: Dinoflagellate cyst ecology: modeling and geological applications. In J. Jansonius and D. C. McGregor (Eds.),
629 *Palynology: principles and applications* (Vol. 3, pp. 1249-1275). American Association of Stratigraphic Palynologists
630 Foundation, 1996.

631 Ding, Z., Yu, Z., Rutter, N. W., and Liu, T.: Towards an orbital time scale for chinese loess deposits. *Quat. Sci. Rev.*, 13(1),
632 39-70, doi: 10.1016/0277-3791(94)90124-4, 1994.

633 Fang, G., Fang, W. D., and Wang, K.: A survey of the study of the South China Sea upper ocean circulation. *Acta Oceanog.*
634 *Tai.*, 37, 1-16, 1998.

635 Felden, J., Möller, L., Schindler, U., Huber, R., Schumacher, S., Koppe, R., Diepenbroek, M., and Glöckner, F. O.: PANGAEA
636 – Data Publisher for Earth & Environmental Science. *Sci. Data*, 10(1), 347, doi: 10.1038/s41597-023-02269-x, 2023.

637 Govin, A., Holzwarth, U., Heslop, D., Ford Keeling, L., Zabel, M., Mulitza, S., Collins, J. A., and Chiessi, C. M.: Distribution
638 of major elements in Atlantic surface sediments (36°N–49°S): Imprint of terrigenous input and continental weathering.
639 *Geochem. Geophys. Geosyst.*, 13(1), doi: 10.1029/2011GC003785, 2012.

640 Grimm, E.: Tilia and TGView 19 version 2.0. 41. software. Springfield, USA: Illinois State Museum, Research and Collection
641 Center, 2015.

642 Hanebuth, T., Stattegger, K., and Grootes, P. M.: Rapid flooding of the Sunda Shelf: A late-glacial sea-level record. *Science*,
643 288(5468), 1033-1035, doi: 10.1126/science.288.5468.1033, 2000.

644 Haynes, J. R.: *Foraminifera*. Palgrave Macmillan London, doi: 10.1007/978-1-349-05397-1, 1981.

645 Holzwarth, U., Esper, O., and Zonneveld, K.: Distribution of organic-walled dinoflagellate cysts in shelf surface sediments of
646 the Benguela upwelling system in relationship to environmental conditions. *Mar. Micropaleontol.*, 64(1–2), 91-119, doi:
647 10.1016/j.marmicro.2007.04.001, 2007.

648 Hu, D., Clift, P. D., Böning, P., Hannigan, R., Hillier, S., Blusztajn, J., Wan, S., and Fuller, D. Q.: Holocene evolution in
649 weathering and erosion patterns in the Pearl River delta. *Geochem. Geophys. Geosyst.*, 14(7), 2349-2368, doi:
650 10.1002/ggge.20166, 2013.

651 Hu, J., Kawamura, H., Hong, H., and Qi, Y.: A review on the currents in the South China Sea: Seasonal circulation, South
652 China Sea warm current and Kuroshio intrusion. *J. Oceanogr.*, 56(6), 607-624, doi: 10.1023/A:1011117531252, 2000.

653 Huang, C., Wu, L., Cheng, J., Qu, X., Luo, Y., Zhang, H., Ye, F., and Wei, G.: Sedimentary responses to climatic variations
654 and Kuroshio intrusion into the northern South China Sea since the last deglaciation. *Global Planet. Change*, 245, 104671,
655 doi: 10.1016/j.gloplacha.2024.104671, 2025.

- 656 Huang, K., You, C., Lin, H., and Shieh, Y.: In situ calibration of Mg/Ca ratio in planktonic foraminiferal shell using time series
657 sediment trap: A case study of intense dissolution artifact in the South China Sea. *Geochem. Geophys. Geosyst.*, 9(4),
658 doi: 10.1029/2007GC001660, 2008.
- 659 Hughen, K. A., Baillie, M. G. L., Bard, E., Warren Beck, J., Bertrand, C. J. H., Blackwell, P. G., Buck, C. E., Burr, G. S.,
660 Cutler, K. B., Damon, P. E., Edwards, R. L., Fairbanks, R. G., Friedrich, M., Guilderson, T. P., Kromer, B., McCormac,
661 G., Manning, S., Bronk Ramsey, C., Reimer, P. J., Reimer, R. W., Remmele, S., Southon, J. R., Stuiver, M., Talamo, S.,
662 Taylor, F. W., Van der Plicht, J., and Weyhenmeyer, C. E.: Marine04 marine radiocarbon age calibration, 0–26 cal kyr
663 BP. *Radiocarbon*, 46(3), 1059-1086, doi: 10.1017/S0033822200033002, 2004.
- 664 Jiwarungrueangkul, T., and Liu, Z.: East Asian monsoon and sea-level controls on clay mineral variations in the southern
665 South China Sea since the Last Glacial Maximum. *Quat. Int.*, 592, 1-11, doi: 10.1016/j.quaint.2021.04.033, 2021.
- 666 Kaars, S. v. d., Wang, X., Kershaw, P., Guichard, F., and Setiabudi, D. A.: A Late Quaternary palaeoecological record from
667 the Banda Sea, Indonesia: patterns of vegetation, climate and biomass burning in Indonesia and northern Australia.
668 *Palaeogeogr., Palaeoclimatol., Palaeoecol.*, 155(1), 135-153, doi: 10.1016/S0031-0182(99)00098-X, 2000.
- 669 Kissel, C., Laj, C., Jian, Z., Wang, P., Wandres, C., and Rebolledo-Vieyra, M.: Past environmental and circulation changes in
670 the South China Sea: Input from the magnetic properties of deep-sea sediments. *Quat. Sci. Rev.*, 236, 106263, doi:
671 10.1016/j.quascirev.2020.106263, 2020.
- 672 Lambeck, K., Rouby, H., Purcell, A., Sun, Y., and Sambridge, M.: Sea level and global ice volumes from the Last Glacial
673 Maximum to the Holocene. *Proc. Natl. Acad. Sci. U. S. A.*, 111(43), 15296-15303, doi: 10.1073/pnas.1411762111, 2014.
- 674 Laskar, J., Robutel, P., Joutel, F., Gastineau, M., Correia, A. C. M., and Levrard, B.: A long-term numerical solution for the
675 insolation quantities of the Earth. *Astronomy & Astrophysics*, 428, 261-285, doi: 10.1051/0004-6361:20041335, 2004.
- 676 Lee, C. M., van Geel, B., and Gosling, W. D.: On the use of spores of coprophilous fungi preserved in sediments to indicate
677 past herbivore presence. *Quaternary*, 5(3), 30, doi: 10.3390/quat5030030, 2022.
- 678 Li, C., Li, Y., Zheng, Y., Yu, S., Tang, L., Li, B., and Cui, Q.: A high-resolution pollen record from East China reveals large
679 climate variability near the Northgrippian-Meghalayan boundary (around 42 years ago) exerted societal influence.
680 *Palaeogeogr., Palaeoclimatol., Palaeoecol.*, 512, 156-165, doi: 10.1016/j.palaeo.2018.07.031, 2018a.
- 681 Li, L., Wang, H., Luo, B., and He, J.: The characterizations and paleoceanographic significances of organic and inorganic
682 carbon in northern South China Sea during past 40 ka. *Mar. Geol. & Qua. Geol.*, 28(6), 79-85, doi:
683 10.3724/sp.J.1140.2008.06079, 2008.
- 684 Li, M., Ouyang, T., Tian, C., Zhu, Z., Peng, S., Tang, Z., Qiu, Y., Zhong, H., and Peng, X.: Sedimentary responses to the East
685 Asian monsoon and sea level variations recorded in the northern South China Sea over the past 3 kyr. *J. Asian Earth Sci.*,
686 171, 213-224, doi: 10.1016/j.jseas.2018.01.001, 2019.
- 687 Li, Z., Pospelova, V., Kawamura, H., Luo, C., Mertens, K. N., Hernández-Almeida, I., Yin, K., Wu, Y., Wu, H., and Xiang,
688 R.: Dinoflagellate cyst distribution in surface sediments from the South China Sea in relation to hydrographic conditions
689 and primary productivity. *Mar. Micropaleontol.*, 159, 101815, doi: 10.1016/j.marmicro.2019.101815, 2020.
- 690 Li, Z., Pospelova, V., Lin, H.-L., Liu, L., Song, B., and Gong, W.: Seasonal dinoflagellate cyst production and terrestrial
691 palynomorph deposition in the East Asian Monsoon influenced South China Sea: A sediment trap study from the
692 Southwest Taiwan waters. *Rev. Palaeobot. Palynol.*, 257, 117-139, doi: 10.1016/j.revpalbo.2018.07.007, 2018b.
- 693 Li, Z., Pospelova, V., Liu, L., Francois, R., Wu, Y., Mertens, K. N., Saito, Y., Zhou, R., Song, B., and Xie, X.: High-resolution
694 reconstructions of Holocene sea-surface conditions from dinoflagellate cyst assemblages in the northern South China Sea.
695 *Mar. Geol.*, 438, 106528, doi: 10.1016/j.margeo.2021.106528, 2021.
- 696 Li, Z., Pospelova, V., Liu, L., Zhou, R., and Song, B.: High-resolution palynological record of Holocene climatic and
697 oceanographic changes in the northern South China Sea. *Palaeogeogr., Palaeoclimatol., Palaeoecol.*, 483, 94-124, doi:
698 10.1016/j.palaeo.2017.03.009, 2017.
- 699 Li, Z., Pospelova, V., Mertens, K. N., Liu, L., Wu, Y., Li, C., and Gu, H.: Evaluation of organic-walled dinoflagellate cyst
700 distributions in coastal surface sediments of the China Seas in relation with hydrographic conditions for
701 paleoceanographic reconstruction. *Quat. Int.*, 661, 60-75, doi: 10.1016/j.quaint.2023.03.007, 2023.
- 702 Lin, D., Chen, M., Yamamoto, M., and Yokoyama, Y.: Millennial-scale alkenone sea surface temperature changes in the
703 northern South China Sea during the past 45,000 years (MD972146). *Quat. Int.*, 333, 207-215, doi:
704 10.1016/j.quaint.2014.03.062, 2014.

- 705 Liu, J., Xiang, R., Chen, Z., Chen, M., Yan, W., Zhang, L., and Chen, H.: Sources, transport and deposition of surface
706 sediments from the South China Sea. *Deep Sea Res. (I Oceanogr. Res. Pap.)*, 71, 92-102, doi: 10.1016/j.dsr.2012.09.006,
707 2013.
- 708 Liu, J., Xiang, R., Kao, S. J., Fu, S., and Zhou, L.: Sedimentary responses to sea-level rise and Kuroshio Current intrusion
709 since the Last Glacial Maximum: Grain size and clay mineral evidence from the northern South China Sea slope.
710 *Palaeogeogr., Palaeoclimatol., Palaeoecol.*, 450, 111-121, doi: 10.1016/j.palaeo.2016.03.002, 2016a.
- 711 Liu, K., Chao, S., Shaw, P., Gong, G., Chen, C., and Tang, T.: Monsoon-forced chlorophyll distribution and primary production
712 in the South China Sea: observations and a numerical study. *Deep Sea Res. (I Oceanogr. Res. Pap.)*, 49(8), 1387-1412,
713 doi: 10.1016/S0967-0637(02)00035-3, 2002.
- 714 Liu, L., Guan, H., Feng, J., Xu, L., Mao, S., and Liu, L.: Composition of glycerol dibiphytanyl glycerol tetraethers (GDGTs)
715 and its responses to paleotemperature and monsoon changes since 31ka in northern South China Sea. *Mar. Geol. & Qua.
716 Geol.*, 40(3), 144-159, doi: 10.16562/j.cnki.0256-1492.2020021101, 2020.
- 717 Liu, Z., Colin, C., Li, X., Zhao, Y., Tuo, S., Chen, Z., Siringan, F. P., Liu, J. T., Huang, C.-Y., You, C.-F., and Huang, K.-F.:
718 Clay mineral distribution in surface sediments of the northeastern South China Sea and surrounding fluvial drainage
719 basins: Source and transport. *Mar. Geol.*, 277(1), 48-60, doi: 10.1016/j.margeo.2010.08.010, 2010.
- 720 Liu, Z., Trentesaux, A., Clemens, S. C., Colin, C., Wang, P., Huang, B., and Boulay, S.: Clay mineral assemblages in the
721 northern South China Sea: implications for East Asian monsoon evolution over the past 2 million years. *Mar. Geol.*,
722 201(1), 133-146, doi: 10.1016/S0025-3227(03)00213-5, 2003.
- 723 Liu, Z., Zhao, Y., Colin, C., Statterger, K., Wiesner, M. G., Huh, C., Zhang, Y., Li, X., Sompongchaiyakul, P., You, C., Huang,
724 C., Liu, J. T., Siringan, F. P., Le, K. P., Sathiamurthy, E., Hantoro, W. S., Liu, J., Tuo, S., Zhao, S., Zhou, S., He, Z.,
725 Wang, Y., Bunsomboonsakul, S., and Li, Y.: Source-to-sink transport processes of fluvial sediments in the South China
726 Sea. *Earth-Sci. Rev.*, 153, 238-273, doi: 10.1016/j.earscirev.2015.08.005, 2016b.
- 727 Luo, C., Chen, C., Xiang, R., Jiang, W., Liu, J., Lu, J., Su, X., Zhang, Q., Yang, Y., and Yang, M.: Study of modern pollen
728 distribution in the northeastern Indian Ocean and their application to paleoenvironment reconstruction. *Rev. Palaeobot.
729 Palynol.*, 256, 50-62, doi: 10.1016/j.revpalbo.2018.05.007, 2018.
- 730 Luo, C., Chen, M., Xiang, R., Liu, J., Zhang, L., and Lu, J.: Comparison of modern pollen distribution between the northern
731 and southern parts of the South China Sea. *Int. J. Biometeorol.*, 59(4), 397-415, doi: 10.1007/s00484-014-0852-2, 2015.
- 732 Luo, C., Jiang, C., Yang, M., Chen, M., Xiang, R., Zhang, L., Liu, J., and Pan, A.: Transportation modes of pollen in surface
733 waters in the South China Sea and their environmental significance. *Rev. Palaeobot. Palynol.*, 225, 95-105, doi:
734 10.1016/j.revpalbo.2015.11.004, 2016.
- 735 Luo, Y., and Sun, X.: Vegetation evolution and millennial-scale climatic fluctuations since Last Glacial Maximum in pollen
736 record from northern South China Sea. *Chin. Sci. Bull.*, 50(8), 793-799, doi: 10.1007/BF03183681, 2005.
- 737 Luo, Y., and Sun, X.: Vegetation evolution and its response to climatic change during 3.15–0.67 Ma in deep-sea pollen record
738 from northern South China Sea. *Chin. Sci. Bull.*, 58(3), 364-372, doi: 10.1007/s11434-012-5374-x, 2013.
- 739 Maher, L.J.: Nomograms for computing 0.95 confidence limits of pollen data. *Rev. Palaeobot. Palynol.*, 13, 85-93, doi:
740 10.1016/0034-6667(72)90038-3, 1972.
- 741 Marret, F., and Zonneveld, K. A. F.: Atlas of modern organic-walled dinoflagellate cyst distribution. *Rev. Palaeobot. Palynol.*,
742 125(1–2), 1-200, doi: 10.1016/S0034-6667(02)00229-4, 2003.
- 743 Matsuoka, K.: Dinoflagellate cysts and pollen in pelagic sediments of the northern part of the Philippin Sea. *Bull., Faculty of
744 Liberal Arts, Nagasaki University. (Natural Science)*, 21(2), 59-70, 1981.
- 745 Meyers, P.A.: Organic geochemical proxies of paleoceanographic, paleolimnologic, and paleoclimatic processes. *Org.
746 Geochem.*, 27, 213-250, doi: 10.1016/S0146-6380(97)00049-1, 1997.
- 747 Milliman, J. D., and Syvitski, J. P. M.: Geomorphic/tectonic control of sediment discharge to the ocean: The importance of
748 small mountainous rivers. *J. Geol.*, 100(5), 525-544, doi: 10.1086/629606, 1992.
- 749 Mooney, S. D., and Tinner, W.: The analysis of charcoal in peat and organic sediments. *Mires Peat*, 7(09), doi:
750 10.19189/001c.128417, 2011.
- 751 Oppo, D. W., and Sun, Y.: Amplitude and timing of sea-surface temperature change in the northern South China Sea: Dynamic
752 link to the East Asian monsoon. *Geology*, 33(10), 785-788, doi: 10.1130/G21867.1, 2005.

753 Schönfeld, J., Alve, E., Geslin, E., Jorissen, F., Korsun, S., and Spezzaferri, S.: The FOBIMO (FORaminiferal Blo-MONitoring)
754 initiative—Towards a standardised protocol for soft-bottom benthic foraminiferal monitoring studies. *Mar.*
755 *Micropaleontol.*, 94-95, 1-13, doi: 10.1016/j.marmicro.2012.06.001, 2012.

756 Smayda, T. J., and Trainer, V. L.: Dinoflagellate blooms in upwelling systems: Seeding, variability, and contrasts with diatom
757 bloom behaviour. *Prog. Oceanogr.*, 85(1), 92-107, doi: 10.1016/j.pocean.2010.02.006, 2010.

758 Stibig, H.-J., Belward, A. S., Roy, P. S., Rosalina-Wasrin, U., Agrawal, S., Joshi, P. K., Beuchle, R., Fritz, S., Mubareka, S.,
759 and Giri, C.: A land-cover map for South and Southeast Asia derived from SPOT-VEGETATION data. *J. Biogeogr.*,
760 34(4), 625-637, doi: 10.1111/j.1365-2699.2006.01637.x, 2007.

761 Stuiver, M., and Reimer, P. J.: Extended 14C Data Base and Revised CALIB 3.0 14C Age Calibration Program. *Radiocarbon*,
762 35(1), 215-230, doi: 10.1017/S0033822200013904, 1993.

763 Sun, X., Li, X., and Beug, H.-J.: Pollen distribution in hemipelagic surface sediments of the South China Sea and its relation
764 to modern vegetation distribution. *Mar. Geol.*, 156(1), 211-226, doi: 10.1016/S0025-3227(98)00180-7, 1999.

765 Sun, X., Li, X., and Chen, H.: Evidence for natural fire and climate history since 37 ka BP in the northern part of the South
766 China Sea. *Sci. China Ser. D-Earth Sci.*, 43(5), 487-493, doi: 10.1007/bf02875310, 2000a.

767 Sun, X., Li, X., Luo, Y., and Chen, X.: The vegetation and climate at the last glaciation on the emerged continental shelf of
768 the South China Sea. *Palaeogeogr., Palaeoclimatol., Palaeoecol.*, 160(3), 301-316, doi: 10.1016/S0031-0182(00)00078-
769 X, 2000b.

770 Sun, X., and Luo, Y.: Pollen record of the last 280 ka from deep sea sediments of the northern South China Sea. *Sci. China*
771 *Ser. D-Earth Sci.*, 44(10), 879-888, doi: 10.1007/BF02907079, 2001.

772 Sun, X., Luo, Y., Huang, F., Tian, J., and Wang, P.: Deep-sea pollen from the South China Sea: Pleistocene indicators of East
773 Asian monsoon. *Mar. Geol.*, 201(1), 97-118, doi: 10.1016/S0025-3227(03)00211-1, 2003.

774 Tang, L., Mao, L., Shu, J., Li, C., Shen, C., and Zhou, Z.: Atlas of Quaternary pollen and spores in China. Science Press and
775 Springer Nature Singapore Pte Ltd, doi: 10.1007/978-981-13-7103-5, 2020.

776 ter Braak, C. J. F., and Smilauer, P.: Canoco reference manual and user's guide: software for ordination, version 5.0.
777 Microcomputer Power, Ithaca, NY, USA. 2012.

778 Tian, J., Huang, E., and Pak, D. K.: East Asian winter monsoon variability over the last glacial cycle: Insights from a latitudinal
779 sea-surface temperature gradient across the South China Sea. *Palaeogeogr., Palaeoclimatol., Palaeoecol.*, 292(1-2), 319-
780 324, doi: 10.1016/j.palaeo.2010.04.005, 2010.

781 Tian, J., Wang, P. X., and Cheng, X. R.: Responses of foraminiferal isotopic variations at ODP Site 1143 in the southern South
782 China Sea to orbital forcing. *Sci. China Ser. D-Earth Sci.*, 47(10), 943-953, doi: 10.1360/03yd0129, 2004.

783 Tian, J., Xie, X., Ma, W., Jin, H., and Wang, P.: X-ray fluorescence core scanning records of chemical weathering and monsoon
784 evolution over the past 5 Myr in the southern South China Sea. *Paleoceanography*, 26(4), doi: 10.1029/2010PA002045,
785 2011.

786 Tyszka, J., Godos, K., Goleń, J., and Radmacher, W.: Foraminiferal organic linings: Functional and phylogenetic challenges.
787 *Earth-Sci. Rev.*, 220, 103726, doi: 10.1016/j.earscirev.2021.103726, 2021.

788 Wan, S., and Jian, Z.: Deep water exchanges between the South China Sea and the Pacific since the last glacial period.
789 *Paleoceanography*, 29(12), 1162-1178, doi: 10.1002/2013PA002578, 2014.

790 Wan, S., Li, A., Clift, P. D., and Stuut, J.-B. W.: Development of the East Asian monsoon: Mineralogical and sedimentologic
791 records in the northern South China Sea since 20 Ma. *Palaeogeogr., Palaeoclimatol., Palaeoecol.*, 254(3), 561-582, doi:
792 10.1016/j.palaeo.2007.07.009, 2007.

793 Wang, C.: The forests of China. Maria Moors Cabot Foundation No.5. Harvard University, Cambridge Mass, USA, 717, 1961.

794 Wang, L., Sarnthein, M., Erlenkeuser, H., Grootes, P. M., Grimalt, J. O., Pelejero, C., and Linck, G.: Holocene variations in
795 Asian monsoon moisture: A bidecadal sediment record from the South China Sea. *Geophys. Res. Lett.*, 26(18), 2889-
796 2892, doi: 10.1029/1999GL900443, 1999.

797 Wang, P., Li, Q., and Tian, J.: Pleistocene paleoceanography of the South China Sea: Progress over the past 20years. *Mar.*
798 *Geol.*, 352, 381-396, doi: 10.1016/j.margeo.2014.03.003, 2014.

799 Wang, P., and Sun, X.: Last glacial maximum in China: comparison between land and sea. *Catena*, 23(3), 341-353, doi:
800 10.1016/0341-8162(94)90077-9, 1994.

801 Wang, P., Wang, B., Cheng, H., Fasullo, J., Guo, Z., Kiefer, T., and Liu, Z.: The global monsoon across time scales:
802 Mechanisms and outstanding issues. *Earth-Sci. Rev.*, 174, 84-121, doi: 10.1016/j.earscirev.2017.07.006, 2017.

803 Wang, X., Sun, X., Wang, P., and Statterger, K.: Vegetation on the Sunda Shelf, South China Sea, during the Last Glacial
804 Maximum. *Palaeogeogr., Palaeoclimatol., Palaeoecol.*, 278(1), 88-97, doi: 10.1016/j.palaeo.2009.04.008, 2009.

805 Wang, Y. J., Cheng, H., Edwards, R. L., An, Z. S., Wu, J. Y., Shen, C.-C., and Dorale, J. A.: A high-resolution absolute-dated
806 late Pleistocene monsoon record from Hulu Cave, China. *Science*, 294(5550), 2345-2348, doi: 10.1126/science.1064618,
807 2001.

808 Wei, G., Liu, Y., Li, X., Shao, L., and Fang, D.: Major and trace element variations of the sediments at ODP Site 1144, South
809 China Sea, during the last 230 ka and their paleoclimate implications. *Palaeogeogr., Palaeoclimatol., Palaeoecol.*, 212(3),
810 331-342, doi: 10.1016/j.palaeo.2004.06.011, 2004.

811 Whitmore, T. C.: Rain forests: Tropical rain forests of the far east. *Science*, 228(4701), 874-875, doi:
812 10.1126/science.228.4701.874, 1985.

813 Williams, G., Fensome, R., and MacRae, R.: *DINOFLAJ3*, 2017.

814 Xie, S.-P., Deser, C., Vecchi, G. A., Ma, J., Teng, H., and Wittenberg, A. T.: Global Warming Pattern Formation: Sea Surface
815 Temperature and Rainfall. *J. Clim.*, 23(4), 966-986, doi: 10.1175/2009JCLI3329.1, 2010.

816 Xie, X., Zheng, H.-B., and Qiao, P.-J.: Millennial climate changes since MIS 3 revealed by element records in deep-sea
817 sediments from northern South China Sea. *Chin. Sci. Bull.*, 59(8), 776-784, doi: 10.1007/s11434-014-0117-9, 2014.

818 Xu, D., Lu, H., Wu, N., Liu, Z., Li, T., Shen, C., and Wang, L.: Asynchronous marine-terrestrial signals of the last deglacial
819 warming in East Asia associated with low- and high-latitude climate changes. *Proc. Natl. Acad. Sci. USA*, 110, 9657 -
820 9662, 10.1073/pnas.1300025110, 2013. Yu, S., Zheng, Z., Chen, F., Jing, X., Kershaw, P., Moss, P., Peng, X., Zhang, X.,
821 Chen, C., Zhou, Y., Huang, K., and Gan, H.: A last glacial and deglacial pollen record from the northern South China
822 Sea: New insight into coastal-shelf paleoenvironment. *Quat. Sci. Rev.*, 157, 114-128, doi:
823 10.1016/j.quascirev.2016.12.012, 2017.

824 Yuan, Y. C., Bu, X. W., Liao, G. H., Lou, R. Y., Su, J. L., and Wang, K. S.: Diagnostic calculation of the upper-layer circulation
825 in the South China Sea during the winter of 1998. *Acta Oceanol. Sin.*, 23(2), 187-199, 2004.

826 Zhang, H., Liu, C., Jin, X., Shi, J., Zhao, S., and Jian, Z.: Dynamics of primary productivity in the northern South China Sea
827 over the past 24,000 years. *Geochem. Geophys. Geosyst.*, 17(12), 4878-4891, doi: 10.1002/2016GC006602, 2016.

828 Zhao, X., Dupont, L., Schefuß, E., Bouimtarhan, I., and Wefer, G.: Palynological evidence for Holocene climatic and
829 oceanographic changes off western South Africa. *Quat. Sci. Rev.*, 165, 88-101, doi: 10.1016/j.quascirev.2017.04.022,
830 2017.

831 Zheng, Z., and Lei, Z. Q.: A 400,000 year record of vegetational and climatic changes from a volcanic basin, Leizhou Peninsula,
832 southern China. *Palaeogeogr., Palaeoclimatol., Palaeoecol.*, 145(4), 339-362, doi: 10.1016/S0031-0182(98)00107-2,
833 1999.

834 Zhong, Y., Chen, Z., Li, L., Liu, J., Li, G., Zheng, X., Wang, S., and Mo, A.: Bottom water hydrodynamic provinces and
835 transport patterns of the northern South China Sea: Evidence from grain size of the terrigenous sediments. *Cont. Shelf
836 Res.*, 140, 11-26, doi: 10.1016/j.csr.2017.01.023, 2017.

837 Zhou, B., Zheng, H., Yang, W., Taylor, D., Lu, Y., Wei, G., Li, L., and Wang, H.: Climate and vegetation variations since the
838 LGM recorded by biomarkers from a sediment core in the northern South China Sea. *J. Quat. Sci.*, 27(9), 948-955, doi:
839 10.1002/jqs.2588, 2012.

840 Zonneveld, K. A. F., Harper, K., Klügel, A., Chen, L., De Lange, G., and Versteegh, G. J. M.: Climate change, society, and
841 pandemic disease in Roman Italy between 200 BCE and 600 CE. *Sci. Adv.*, 10(4), eadk1033, doi: 10.1126/sciadv.adk1033,
842 2024.

843 Zonneveld, K. A. F., Marret, F., Versteegh, G. J. M., Bogus, K., Bonnet, S., Bouimtarhan, I., Crouch, E., de Vernal, A.,
844 Elshanawany, R., Edwards, L., Esper, O., Forke, S., Grøsfjeld, K., Henry, M., Holzwarth, U., Kielt, J. F., Kim, S.,
845 Ladouceur, S., Ledu, D., Chen, L., Limoges, A., Londeix, L., Lu, S. H., Mahmoud, M. S., Marino, G., Matsouka, K.,
846 Matthiessen, J., Mildenhall, D. C., Mudie, P., Neil, H. L., Pospelova, V., Qi, Y., Radi, T., Richerol, T., Rochon, A.,
847 Sangiorgi, F., Solignac, S., Turon, J. L., Verleye, T., Wang, Y., Wang, Z., and Young, M.: Atlas of modern dinoflagellate
848 cyst distribution based on 2405 data points. *Rev. Palaeobot. Palynol.*, 191(0), 1-197, doi: 10.1016/j.revpalbo.2012.08.003,
849 2013.

850 Zonneveld, K. A. F., and Pospelova, V.: A determination key for modern dinoflagellate cysts. *Palynology*, 39(3), 387-409, doi:
851 10.1080/01916122.2014.990115, 2015.

852 Zonneveld, K. A. F., Versteegh, G., and Kodrans-Nsiah, M.: Preservation and organic chemistry of Late Cenozoic organic-
853 walled dinoflagellate cysts: A review. *Mar. Micropaleontol.*, 68(1–2), 179-197, doi: 10.1016/j.marmicro.2008.01.015,
854 2008.